AAS 17-402

ADAPTIVE FILTERING FOR MANEUVER-FREE ANGLES-ONLY NAVIGATION IN ECCENTRIC ORBITS

Joshua Sullivan[*], **Simone D'Amico**[†]

This paper addresses the design and validation of accurate estimation architectures for autonomous angles-only navigation in orbits of arbitrary eccentricity. The proposed filtering strategies overcome the major deficiencies of existing approaches in the literature, which mainly focus on applications in near-circular orbits and generally suffer from poor dynamical observability due to linearizing the dynamics and measurement models implemented in the filter. Consequently, traditional angles-only navigation solutions require conducting known orbital maneuvers to reconcile the ambiguous relative range. In contrast, the algorithms developed in this work enable accurate maneuver-free reconstruction of the relative orbital motion. This is done through the full exploitation of nonlinearities in the measurement model using the unscented Kalman filter to improve dynamical observability and filter performance. The filter estimates mean relative orbit elements, adopting a state transition matrix subject to secular and long-period J_2 perturbation effects to decouple observable from unobservable parameters. The complete state is then reconciled with the angle measurements in the measurement model through a nonlinear transformation which includes the conversion from mean to osculating orbital elements. The resulting linear dynamics model is supplemented by a covariance-matching approach to online adaptive process noise tuning to increase performance at minimal computational complexity. Finally, the estimation architecture is completed by a novel deterministic algorithm for batch initial relative orbit determination to accurately initialize the sequential filters.

INTRODUCTION

Future space missions involving the interaction of multiple satellites present increasingly demanding relative navigation requirements which must be achieved autonomously using limited onboard resources. The research presented in this paper considers a particularly useful relative navigation scenario wherein an observing spacecraft is navigating with respect to a target space object at large separations (several kilometers) using only bearing angles obtained by a single onboard camera. This so-called angles-only navigation provides an inherently passive, robust, and high-dynamic-range capability which uses simple sensors that are already on board most spacecraft. Accordingly, angles-only navigation represents a clear enabling technology for a variety of advanced distributed space system (DSS) missions, including robust autonomous rendezvous and docking, improved space situational awareness, advanced distributed aperture science, and on-orbit servicing of non-cooperative spacecraft.[1] In line with the terminology of the last application, this paper denotes the observing spacecraft as "the servicer" and treats its orbit as the reference about which to describe the relative orbital motion of the target.

The angles-only navigation problem has been explored in several research studies, both from the perspective of developing and evaluating the analytical framework for relative state estimation using bearing angles, and also in the lens of designing and achieving in-flight demonstrations. In general, the majority of previous literature operates under the well-documented claim that the angles-only navigation problem is not fully observable due to a lack of explicit relative range information. The work of Woffinden and Geller[2] clarify

[*] Doctoral Candidate, Stanford University, Department of Aeronautics and Astronautics, Space Rendezvous Laboratory, Durand Building, 496 Lomita Mall, Stanford, CA 94305-4035

[†] Assistant Professor, Stanford University, Department of Aeronautics and Astronautics, Space Rendezvous Laboratory, Durand Building, 496 Lomita Mall, Stanford, CA 94305-4035

this claim by providing closed-form sufficient conditions for observability using a linearized relative motion model in rectilinear coordinates. The conclusion is that, when formulating the angles-only navigation dynamical system, using purely linear models for the dynamics and measurements yields an unobservable system whereby the complete relative motion state cannot be reconstructed from sequences of bearing angles. Gaias et al.[3] explore the use of a relative orbital element (ROE) based description for the relative motion, and show an improved physical interpretation wherein the unobservability problems are confined to a single state element which best approximates the ambiguous relative range. Furthermore, the inclusion of the J_2 perturbation is shown to improve the mathematical metrics for observability, namely through decreasing the condition number of the so-called observability matrix. Still, the most common method employed by researchers to mitigate the unobservability, and the one taken by Woffinden and Geller[4] and Gaias et al., is to conduct designated orbital maneuvers which produce a known variation to the natural bearing angle trends. Instead, recent work by Sullivan et al.[5] has formulated a novel procedure for angles-only navigation that does not require designated orbital maneuvering for successful relative motion estimation in circular, low Earth orbits (LEO). The authors leverage the same ROE state as discussed above, and institute an estimation architecture which includes nonlinear effects related to the mean-to-osculating transformation when mapping variations of the measured bearing angles to variations in the modeled J_2-perturbed relative motion. However, several limitations exist within that research, including inconsistent filter performance for several common relative motion configurations, slow convergence rates for the estimation of the ROE state, and sensitivity to the selected filter tuning parameters.

In the framework of the ARGON and AVANTI in-flight demonstrations, the research studies of D'Amico et al.[6] and Gaias et al.[7] provide compelling evidence showing that the unobservability decoupling and practical collision-avoidance constraints based on the E/I-vector separation principle[8] enable successful reconstruction of the ROE state when applied in conjunction with orbital maneuvers. The ARGON mission was able to demonstrate angles-only rendezvous from tens of kilometers down to two kilometers separation in LEO using ground-in-the-loop image processing and relative orbit determination. Instead, the ongoing AVANTI mission is targeting autonomous angles-only navigation and rendezvous with a designated navigation filter using the ROE to estimate the J_2- and differential-drag-perturbed relative motion in LEO. These demonstrations provide useful insight into the constraints imposed by a real-world implementation of angles-only relative navigation.

As a final consideration, the problem of angles-only initial relative orbit determination (IROD) is of great utility to both general space situational awareness and to the completion of an encompassing angles-only sequential filtering framework. An accurate and computationally efficient IROD tool can provide the necessary initialization to begin sequential angles-only filtering. In this context, Sullivan et al.[5] develop an IROD tool that uses a reduced set of ROE non-dimensionalized by the relative mean longitude to estimate the shape and orientation of the relative motion in circular, unperturbed orbits. That method neglects the dynamical evolution of the reduced ROE set and requires prior knowledge on the relative separation to fully initialize the sequential estimation of the ROE state. Instead, Geller and Lovell[9] explore the use of a second-order expansion of the measurement model, combined with the linear Hill-Clohessy-Wiltshire (HCW) dynamics model in spherical coordinates, to provide an approximate IROD solution for unperturbed, circular orbits. The thesis work of Hebert[10] investigates a methodology that uses successive orbital maneuvers to iteratively solve for the initial relative state in circular, unperturbed orbits. Finally, the previously mentioned ARGON and AVANTI missions rely on a priori orbital knowledge of the target provided by NORAD Two Line Elements (TLE) and designated radar campaigns, respectively, to fully initialize the estimation procedures without using bearing angle measurements at all.

This paper primarily addresses the limitations of the previous maneuver-free approach of Sullivan et al.[5] through the following main contributions to the state-of-the-art. First, a novel deterministic method for angles-only initial relative orbit determination is developed which now captures J_2-perturbed dynamics for orbits of arbitrary eccentricity. This method reduces the amount of bearing angle measurements required for high performance, minimizes the reliance on a priori target orbit knowledge, and provides accurate initial ROE estimates to the sequential filter without using orbital maneuvers. Then, an innovative design procedure is conducted with the objective of developing a completely maneuver-free sequential state estimation archi-

tecture that yields accurate and robust performance with minimal increase in complexity for eccentric orbit scenarios. The filtering approaches developed in this paper are founded on nonlinear variants of the seminal Kalman filter (KF) methodology originally presented by Rudolf Kalman[11–13] in the context of estimation for linear systems. Notably, the *extended* KF (EKF) discussed by Bucy[14] and the *unscented* KF (UKF) presented by Julier and Uhlmann[15] are considered since they allow the powerful linear KF approach to be applied to systems with nonlinear dynamics and/or measurement models. In an effort to retain simplicity of the filtering frameworks, purely linear dynamics models which capture the secular J_2 perturbation effects on the mean ROE are implemented instead of complex numerical integration methods for nonlinear dynamics propagation. To overcome the tight observability constraints imposed by maneuver-free angles-only navigation, the filter measurement model retains an appropriate nonlinear mean-to-osculating transformation that better relates separation-dependent osculating effects observed in the measured bearing angle trends to variations in the estimated ROE state parameters. With these fundamental considerations handled, the scope of the design process transitions to improving filter accuracy and robustness. To that end, an inventive and simplistic framework is developed and implemented to estimate the ROE and camera sensor biases. At the core of this formulation is an adaptive angles-only filtering strategy which tunes the process noise statistics online to improve filter process modeling and proactively minimize sensitivity to filter noise statistics parameters that are instead often chosen through trial-and-error. The overall result is a set of estimation architectures which have been pragmatically improved to maximize the potential dynamical observability and filtering performance while still decoupling the navigation process from the maneuver-planning problem. Finally, the performance of each estimator design is validated in high-fidelity against rigorous numerically propagated force models, subject to realistic constraints on sensor performance.

This introduction is followed by a discussion of the necessary mathematical preliminaries which highlight the overall dynamical system formulation and provide the foundation for estimating the relative motion as encoded by a set of relative orbital elements. The problem of filter initialization through initial relative orbit determination is addressed in the subsequent section, followed by the design and validation of multiple maneuver-free navigation filters. Finally, the closing section offers concluding remarks and lessons learned on the topic.

MATHEMATICAL PRELIMINARIES

The angles-only navigation problem studied in this paper involves estimating the relative state of a target space object with respect to an observing servicer spacecraft using only bearing angle measurements from a camera sensor on board the servicer spacecraft. Eccentric orbit scenarios are considered which emulate far- to mid-range operations, with separations ranging from tens of kilometers to a few hundred meters. While it is assumed that the initial relative state is unknown, there may be coarse a priori information available to initialize the navigation procedure. The estimation problem is fully posed by the received measurements and by the choice of state to be reconstructed.

The available measurements are synchronous bearing angles, here denoted as the azimuth, α, and elevation, ϵ, which subtend the rectilinear relative position vector pointing from the servicer spacecraft to the target object, $\delta\boldsymbol{r}^{\mathcal{C}} = \left(\delta r_x^{\mathcal{C}},\ \delta r_y^{\mathcal{C}},\ \delta r_z^{\mathcal{C}}\right)^{\mathrm{T}}$. The superscript $\mathcal{C}$ indicates that this line-of-sight (LOS) vector is described in the servicer camera frame, which has a known orientation with respect to the servicer reference frame. The servicer reference frame is denoted as the RTN frame and is compactly indicated with superscript $\mathcal{R}$. The RTN frame is centered on and rotates with the servicer spacecraft, and is composed of orthogonal basis vectors $\hat{\boldsymbol{R}}$ directed along the servicer absolute position vector, $\hat{\boldsymbol{N}}$ in the direction of the servicer orbital angular momentum vector, and $\hat{\boldsymbol{T}} = \hat{\boldsymbol{N}} \times \hat{\boldsymbol{R}}$ completes the right-handed triad. Since far- to mid-range space rendezvous scenarios often begin from large separations in the (anti-)flight direction, this paper assumes without loss of generality a camera with boresight, $\hat{z}^{\mathcal{C}}$, aligned in the anti-velocity direction, $\hat{y}^{\mathcal{C}}$ aligned with the angular momentum vector of the servicer orbit ($\hat{\boldsymbol{N}}$), and $\hat{x}^{\mathcal{C}}$ completing the right-handed triad. Note that this orientation differs from the RTN frame only by a rotation about $\hat{\boldsymbol{N}}$ by the instantaneous servicer flightpath angle, φ_{fpa}. Figure 1 depicts the relationship between the bearing angles and the LOS vector, as well as the relevant camera and RTN frames.

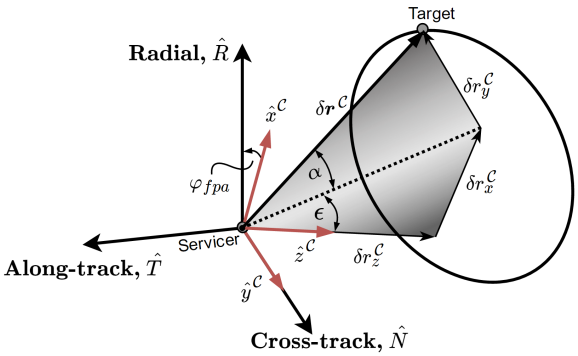

Figure 1: Definition of bearing angles with respect to camera and RTN frame axes.

The nonlinear measurement model that expresses the bearing angles as functions of the relative camera frame position is given by

$$\boldsymbol{y} = \begin{pmatrix} \alpha \\ \epsilon \end{pmatrix} = \begin{pmatrix} \arcsin\left(\delta r_y^{\mathcal{C}} / ||\delta \boldsymbol{r}^{\mathcal{C}}||\right) \\ \arctan\left(\delta r_x^{\mathcal{C}} / \delta r_z^{\mathcal{C}}\right) \end{pmatrix} = \boldsymbol{h}(\delta \boldsymbol{r}^{\mathcal{C}}, t) \tag{1}$$

With regard to choosing the state variables to be estimated, several alternative representations exist for describing the evolution of the relative orbital motion, including relative position and velocity components in the servicer RTN frame, combinations of servicer and target orbital elements, Euler parameters, epicyclic parameters, and spheroidal elements. Sullivan et al.[16] provide a detailed survey of the relative motion dynamics models built from several of these parameterizations. For this paper, a state representation consisting of mean quasi-nonsingular ROE composed of the following combination of mean absolute orbital elements is adopted

$$\delta \boldsymbol{x}_{\text{oe}} = \begin{pmatrix} \delta a \\ \delta \lambda \\ \delta e_x \\ \delta e_y \\ \delta i_x \\ \delta i_y \end{pmatrix} = \begin{pmatrix} \delta a \\ \delta \lambda \\ \delta e c_\varphi \\ \delta e s_\varphi \\ \delta i c_\vartheta \\ \delta i s_\vartheta \end{pmatrix} = \begin{pmatrix} (a_t - a_s)/a_s \\ (u_t - u_s) + c_{i_s}(\Omega_t - \Omega_s) \\ e_t c_{\omega_t} - e_s c_{\omega_s} \\ e_t s_{\omega_t} - e_s s_{\omega_s} \\ i_t - i_s \\ s_{i_s}(\Omega_t - \Omega_s) \end{pmatrix} \tag{2}$$

Here, $u = M + \omega$ is the mean argument of latitude, a, e, i, Ω, ω, and M are the classical Keplerian orbital elements, and c and s denote the cosine and sine of the argument in the subscript, respectively. In this parameterization, δa is the relative semi-major axis, $\delta\lambda$ is the relative mean longitude, $\delta \boldsymbol{e}$ is the relative eccentricity vector with magnitude δe and phase φ, and $\delta \boldsymbol{i}$ is the relative inclination vector with magnitude δi and phase ϑ. This state remains valid for circular reference orbits, but is singular for reference orbits that are strictly equatorial. In addition to this quasi-nonsingular state, Koenig et al.[17] also consider a set of fully singular and fully nonsingular ROE, and provide conversions between the three state representations. In this paper, a distinction is made between *mean* elements, which describe the orbital motion subject to an averaged perturbation effect, and *osculating* elements which instead describe the orbit that is instantaneously coincident with the true perturbed trajectory. Hereafter, $\widetilde{(\cdot)}$ will explicitly indicate osculating elements or relative states composed of osculating elements (for example, $\widetilde{a}$, $\delta\widetilde{\boldsymbol{x}}_{\text{oe}}$, etc.) to distinguish from mean elements.

An application of averaging theory, in conjunction with the Gauss Variational Equations (GVE) and Lagrange Planetary Equations (LPE), provides an analytical framework for describing the secular evolution of the mean ROE due to conservative and non-conservative perturbations. Several authors have leveraged this advantage to solve the variational equations in closed-form, providing relative motion dynamics models that are valid in the presence of higher-order geopotential, third-body gravity, atmospheric drag, and solar radiation pressure effects.[17–19] Furthermore, D'Amico[8,20] has extensively formulated a powerful connection

relating the mean ROE state of Eq. (2) to the relative motion geometry in circular orbits. The utility of that development is demonstrated in pragmatic guidance and control strategies that account for the slow ROE time-variation under the influence of the J_2 Earth oblateness perturbation. Accordingly, the use of the same ROE in this paper is further motivated by an interest in extending these insightful geometric interpretations to the more general eccentric orbit cases.

In addition to reconstructing the relative motion ROE state, the angles-only scenario can be formulated to estimate other useful quantities. For this paper, the complete estimation state is

$$\boldsymbol{x}(t) = \begin{pmatrix} \delta\boldsymbol{x}_{\text{oe}} \\ \boldsymbol{b} \end{pmatrix} \in \mathbb{R}^8 \tag{3}$$

where $\boldsymbol{b} = (b_\alpha \ , \ b_\epsilon)^{\text{T}} \in \mathbb{R}^2$ is the vector of azimuth and elevation sensor biases.

With the filter state chosen and the observables fixed, the foundation for the estimation problem is now formulated with an appropriate dynamical system representation. In the general angles-only relative navigation problem, both the dynamics describing the relative motion and the measurement model relating state elements to observations (see Eq. 1) are nonlinear. Accordingly, the EKF and UKF architectures are employed since they include modifications to the linear KF algorithm to account for nonlinear systems. The EKF variant requires a first-order truncation of the dynamics and measurement model Taylor series expansions, so the following section proceeds with the development of a linear dynamical system representation for the estimation problem. The time-evolution of the complete estimation state is thus governed by the system of differential equations

$$\dot{\boldsymbol{x}}(t) = \boldsymbol{A}(t)\boldsymbol{x}(t) + \boldsymbol{B}(t)\boldsymbol{u}(t) + \boldsymbol{w}(t) \tag{4}$$

In the above equation, $\boldsymbol{A}(t) \in \mathbb{R}^{8\times8}$ is the so-called plant matrix which captures the natural dynamics of the system, $\boldsymbol{B}(t) \in \mathbb{R}^{8\times3}$ is the input sensitivity matrix relating RTN-frame control inputs, $\boldsymbol{u}(t) \in \mathbb{R}^3$, to the state evolution, and $\boldsymbol{w}(t) \in \mathbb{R}^8$ is zero-mean Gaussian white process noise (i.e., $\boldsymbol{w}(t) \sim \mathcal{N}(\boldsymbol{0}_{8\times1}, \boldsymbol{Q}(t))$ with covariance matrix $\boldsymbol{Q}(t) \in \mathbb{R}^{8\times8}$). Superposition of the zero input response and zero state response provides a complete solution to the above set of differential equations

$$\boldsymbol{x}(t) = \boldsymbol{\Phi}(t, t_0)\boldsymbol{x}(t_0) + \int_{t_0}^{t} \boldsymbol{\Phi}(t, \tau)\boldsymbol{B}(\tau)\boldsymbol{u}(\tau)d\tau \tag{5}$$

The state transition matrix (STM), $\boldsymbol{\Phi}(t, t_0) \in \mathbb{R}^{8\times8}$, maps the state from time t_0 to time t, and has the following structure composed of the individual STMs for each subset of the total estimation state

$$\boldsymbol{\Phi}(t, t_0) = \begin{bmatrix} \boldsymbol{\Phi}_{\text{oe}} & \boldsymbol{0}_{6\times2} \\ \boldsymbol{0}_{2\times6} & \boldsymbol{\Phi}_b \end{bmatrix} \tag{6}$$

Each of the STMs in the above equation will be thoroughly detailed in the following sections. Note that $\boldsymbol{\Phi}_{\text{oe}}$, $\boldsymbol{\Phi}_b$ describe the direct propagation of their associated state subset from a previous time.

By expanding the nonlinear measurement model of Eq. (1) in a first-order Taylor series about the reference state, a linear measurement model is formulated which takes the form

$$\boldsymbol{y}(t) = \boldsymbol{C}(t)\boldsymbol{x}(t) + \boldsymbol{\nu}(t) \tag{7}$$

Here, $\boldsymbol{y}(t) \in \mathbb{R}^2$ is the vector of modeled azimuth and elevation angles, $\boldsymbol{C}(t) \in \mathbb{R}^{2\times8}$ is the measurement sensitivity matrix which relates variations in the propagated state $\boldsymbol{x}(t)$ to the modeled measurements, and $\boldsymbol{\nu}(t) \in \mathbb{R}^2$ is zero-mean Gaussian white measurement noise (i.e., $\boldsymbol{\nu}(t) \sim \mathcal{N}(\boldsymbol{0}_{2\times1}, \boldsymbol{R}(t))$ with covariance matrix $\boldsymbol{R}(t) \in \mathbb{R}^{2\times2}$).

Since this paper is concerned with maneuver-free estimation, the control matrix, $\boldsymbol{B}(t)$, is not developed. Similar to Eq. (6), the measurement sensitivity matrix, $\boldsymbol{C}(t)$, can be decomposed into a form with components corresponding to subsets of the complete estimation state

$$\boldsymbol{C}(t) = \begin{bmatrix} \boldsymbol{C}_{\text{oe}} & \boldsymbol{C}_b \end{bmatrix} \tag{8}$$

Relative Orbital Element Subset

The necessary system matrices for the relative motion state subset will now be developed in detail under the assumption of linear relative motion with respect to a servicer in an arbitrarily eccentric orbit. The work of Gaias et al.[7] makes use of a relative motion model which includes the effects of the Earth oblateness J_2 perturbation and time-varying atmospheric drag effects[21] for angles-only navigation in circular orbit. For this paper, however, the relative motion STM is developed to incorporate only the dominant J_2 perturbation effects in eccentric orbit, which in general cause short- and long-period oscillations as well as secular drifts in the orbital elements. By substituting the first-order averaged J_2-perturbed potential into the LPE and effectively time-averaging the ROE variational equations, only the secular and long-period effects are captured in the dynamics model. Koenig et al.[17] have formalized a modular procedure to build the STM for the time-varying system through a coordinate transformation to an intermediary time-invariant system. The resulting STM for propagating the ROE evolution over the interval $[t,\ t+\Delta t]$ is given by

$$\boldsymbol{\Phi}_{\text{oe}} = \begin{bmatrix} 1 & 0 & 0 & 0 & 0 & 0 \\ -(\frac{7}{2}\kappa EP - \frac{3}{2}n)\Delta t & 1 & \kappa e_{x0} FGP\Delta t & \kappa e_{y0} FGP\Delta t & -\kappa FS\Delta t & 0 \\ \frac{7}{2}\kappa e_{yf} Q\Delta t & 0 & c_{\dot{\omega}\Delta t} - 4\kappa e_{x0} e_{yf} GQ\Delta t & -s_{\dot{\omega}\Delta t} - 4\kappa e_{y0} e_{yf} GQ\Delta t & 5\kappa e_{yf} S\Delta t & 0 \\ -\frac{7}{2}\kappa e_{xf} Q\Delta t & 0 & s_{\dot{\omega}\Delta t} + 4\kappa e_{x0} e_{xf} GQ\Delta t & c_{\dot{\omega}\Delta t} + 4\kappa e_{y0} e_{xf} GQ\Delta t & -5\kappa e_{xf} S\Delta t & 0 \\ 0 & 0 & 0 & 0 & 1 & 0 \\ \frac{7}{2}\kappa S\Delta t & 0 & -4\kappa e_{x0} GS\Delta t & -4\kappa e_{y0} GS\Delta t & 2\kappa T\Delta t & 1 \end{bmatrix} \tag{9}$$

where

$$\begin{aligned} &\gamma = \frac{3}{4} J_2 R_e^2 \sqrt{\mu} \quad \eta = \sqrt{1 - ||\boldsymbol{e}||^2} \quad \kappa = \frac{\gamma}{a^{7/2}\,\eta^4} \quad G = \frac{1}{\eta^2} \\ &E = 1 + \eta \qquad F = 4 + 3\eta \qquad T = s_i^2 \qquad \Delta t = t - t_0 \\ &P = 3c_i^2 - 1 \qquad Q = 5c_i^2 - 1 \qquad S = s_{2i} \qquad \dot{\omega} = kQ \end{aligned} \tag{10}$$

Earth's equatioral radius and gravitational parameter are denoted as R_e and μ, respectively, n is the servicer mean motion, and $\boldsymbol{e} = (e_x,\ e_y)^{\text{T}} = e_s\,(c_{\omega_s},\ s_{\omega_s})^{\text{T}}$ denotes the servicer eccentricity vector. From now on, the absolute orbital elements that appear will always belong to the servicer spacecraft, so the subscript s will be dropped for ease of notation.

The structure of this STM provides insight into the evolution of the ROE due to J_2 which is useful for reconciling potential observability issues that arise due to only using bearing angle measurements. First, both $\delta\lambda$ and δi_y display constant drift, with the former resulting from combined Keplerian orbital motion and J_2 and the latter from only J_2. Additionally, the evolution of the relative eccentricity vector is marked by a secular drift perpendicular to the servicer eccentricity vector and a circular precession. An illustration of these trends is provided in Figure 2. While the established dynamics model only captures these secular and long-period variations in the mean ROE, it will be later shown that a strategic linearization of the measurement model allows the osculating effect of the short-period oscillations to be reincorporated in the estimation process.

The measurement sensitivity matrix relating ROE variations to bearing angle variations, $\boldsymbol{C}_{\text{oe}}$, is developed using the following series of partial derivatives

$$\boldsymbol{C}_{\text{oe}}(\delta\boldsymbol{x}_{\text{oe}}(t)) = \frac{\partial \boldsymbol{y}}{\partial \delta\boldsymbol{x}_{\text{oe}}}\bigg|_{\delta\boldsymbol{x}_{\text{oe}}^{\text{ref}}} = \frac{\partial \boldsymbol{y}}{\partial \delta\boldsymbol{r}^{\mathcal{C}}} \cdot \frac{\partial \delta\boldsymbol{r}^{\mathcal{C}}}{\partial \delta\boldsymbol{r}^{\mathcal{R}}} \cdot \frac{\partial \delta\boldsymbol{r}^{\mathcal{R}}}{\partial \delta\boldsymbol{x}_{\text{oe}}}\bigg|_{\delta\boldsymbol{x}_{\text{oe}}^{\text{ref}}} \tag{11}$$

The rightmost term represents a linear mapping from ROE to relative position in the servicer RTN frame. As previously stated, D'Amico[20] has developed this mapping under the assumption of circular orbits by proving a first-order equivalence between the ROE of Eq. (2) and the integration constants of the HCW model.

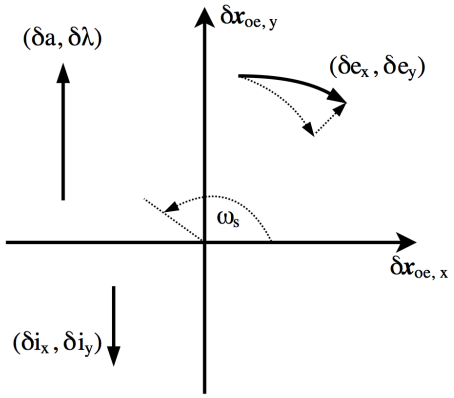

Figure 2: Secular and long-period variations of the mean ROE due to the J_2 perturbation.[17]

That formulation leads to improved geometric insight whereby components of the ROE state correspond to features of the relative orbit trajectory. An analogous mapping with similar geometric benefit for the case of an arbitrarily eccentric reference orbit is derived by Sullivan and D'Amico.[22] In that paper, it is shown that a particular combination of the ROE share a first-order equivalence with the integration constants of the Yamanaka-Ankersen dynamics model, which leads to the following mapping

$$\left.\frac{\partial \delta \boldsymbol{r}^{\mathcal{R}}}{\partial \delta \boldsymbol{x}_{\text{oe}}}\right|_{\delta \boldsymbol{x}_{\text{oe}}^{\text{ref}}} = \left.\frac{\partial \delta \boldsymbol{r}^{\mathcal{R}}}{\partial \delta \boldsymbol{x}_{\text{oe}}}\right|_{\mathbf{0}} = r(f)\Psi_1\Psi_2 \tag{12}$$

where

$$\Psi_1 = \begin{bmatrix} 1 & 0 & -kc_f & -ks_f & 0 & 0 \\ 0 & 1 & (k+1)s_f & -(k+1)c_f + \frac{e}{2} & 0 & 0 \\ 0 & 0 & 0 & 0 & s_\theta & -c_\theta \end{bmatrix} \tag{13}$$

$$\Psi_2 = \begin{bmatrix} 1 & 0 & 0 & 0 & 0 & 0 \\ 0 & \xi & -\dfrac{(1-\xi)s_\omega}{e} & \dfrac{(1-\xi)c_\omega}{e} & 0 & \cot i \\ 0 & 0 & \dfrac{c_\omega}{\eta^2} & \dfrac{s_\omega}{\eta^2} & 0 & 0 \\ 0 & -\dfrac{e}{\eta^3} & -\dfrac{s_\omega}{\eta^3} & \dfrac{c_\omega}{\eta^3} & 0 & \dfrac{e\cot i}{\eta^3} \\ 0 & 0 & 0 & 0 & 1 & 0 \\ 0 & 0 & 0 & 0 & 0 & 1 \end{bmatrix} \tag{14}$$

where f and $\theta = f + \omega$ are the servicer true anomaly and true argument of latitude, $r(f)$ denotes the servicer orbital radius, $k = 1 + ec_f$, and the auxiliary eccentricity factor, ξ, is defined as

$$\xi = \frac{1 + \frac{1}{2}e^2}{\eta^3} \tag{15}$$

The center term of $\boldsymbol{C}_{\text{oe}}$ in Eq. (11) corresponds to the attitude of the camera frame with respect to the servicer RTN frame, which is assumed to be known to the accuracy of commercially available attitude determination systems. Recalling the geometry of Figure 1, the nominal camera frame attitude with respect to the

RTN frame is represented as the combined rotation matrix

$$\frac{\partial \delta \boldsymbol{r}^{\mathcal{C}}}{\partial \delta \boldsymbol{r}^{\mathcal{R}}} = \boldsymbol{R}^{\mathcal{C}}_{\mathcal{R}} = \begin{bmatrix} 1 & 0 & 0 \\ 0 & 0 & 1 \\ 0 & -1 & 0 \end{bmatrix} \begin{bmatrix} c_{\varphi_{fpa}} & s_{\varphi_{fpa}} & 0 \\ -s_{\varphi_{fpa}} & c_{\varphi_{fpa}} & 0 \\ 0 & 0 & 1 \end{bmatrix} \tag{16}$$

where the right matrix imposes a rotation by the flightpath angle, φ_{fpa}, from the RTN frame to the frame containing the velocity vector direction, and the left matrix describes the permutation of the camera axes with respect to that latter frame.

Finally, the leftmost term of Eq. (11) is the sensitivity of the modeled measurements with respect to variations in the camera frame relative position vector. Gaias et al.[3] give the expression in terms of modeled bearing angles as

$$\frac{\partial \boldsymbol{y}}{\partial \delta \boldsymbol{r}^{\mathcal{C}}} = \frac{1}{||\delta \boldsymbol{r}^{\mathcal{C}}||} \begin{bmatrix} -\sin\alpha\sin\epsilon & \cos\alpha & -\sin\alpha\cos\epsilon \\ \sec\alpha\cos\epsilon & 0 & -\sec\alpha\sin\epsilon \end{bmatrix} \tag{17}$$

In order to compute the modeled bearing angles needed in Eq. (17), it is necessary to map the propagated ROE state to relative position in the servicer RTN frame and apply Eq. (16) followed by Eq. (1). Multiple linear and nonlinear mappings are considered by Sullivan et al.[5] in the context of an observability assessment and angles-only navigation filter validation in circular orbits. The approach taken in this paper leverages the insight gained from that research to formulate the necessary mapping in an effort to maximize estimation accuracy and potential filter observability. Accordingly, a nonlinear mapping is chosen whereby the estimated mean ROE and the known mean absolute orbital elements of the servicer are used to calculate the mean absolute orbital elements of the target (see Eq. 2). These mean absolute orbital element sets can then be converted to corresponding osculating sets through the mean-to-osculating transformation offered by Schaub and Junkins [23, App. F] and then used to compute the absolute position and velocity of the servicer and target. Finally, the relative position is calculated and mapped to the servicer RTN frame. This complete mapping takes a functional form $\boldsymbol{g} : \mathbb{R}^6 \mapsto \mathbb{R}^3$ given by

$$\delta r_j^{\mathcal{R}} = g_j(\delta \boldsymbol{x}_{\text{oe}}(t), \text{oe}_s(t)) \tag{18}$$

where $\text{oe}_s(t)$ is the servicer absolute orbital element state at time t, and $j \in \{R,\, T,\, N\}$ indexes the components of the RTN position vector.

Recall that the chosen dynamic model includes only the secular and long-period variations of the mean ROE due to J_2 and neglects the short-period oscillations characterizing the true osculating perturbed relative motion. In general, the short-period relative motion variations induced by perturbations are proportional to the separation (i.e, as separation decreases, differences in the osculating short-period orbital variations of the target and servicer decrease, and vice versa). Accordingly, these osculating characteristics necessarily encode information about the separation that can be leveraged in the measurement modeling. Since the received sensor measurements are inherently osculating, capturing these periodic effects with the aforementioned mean-to-osculating transformation (which is nonlinear in terms of separation) is expected to improve the ability to reconcile range observability problems, as well as the ability to accurately map bearing angle measurement variations to variations in the full ROE state. That transformation is linear in J_2, so errors of $O(J_2^2)$ are expected. As an interesting consideration, one might attempt to confront the observability problem of angles-only estimation using the Gim-Alfriend (GA) dynamics model,[24,25] which captures the evolution of the mean orbital element differences (OED) subject to secular J_2 perturbation effects in arbitrarily eccentric orbits, and subsequently applies a mapping to osculating OED followed by a mapping to relative position and velocity elements. However, since the mappings employed in the GA method to account for the mean-to-osculating transformation are linearized with respect to separation (as well as J_2), the same range-reconciling benefits as the approach suggested in this paper are not obtained.

Sensor Biases Subset

Sensor biases are reasonably assumed to be stationary, band-limited noise processes that are well-modeled as exponentially autocorrelated random variables (i.e., first-order Gauss-Markov processes), with known time

constant, τ_b. Accordingly, the random process is described by the decaying exponential function

$$\psi(\tau) = \exp\left(-\Delta t/\tau\right) \tag{19}$$

which is used to express the appropriate STM for the biases as

$$\boldsymbol{\Phi}_b = \begin{bmatrix} \psi(\tau_b) & 0 \\ 0 & \psi(\tau_b) \end{bmatrix} \tag{20}$$

Note that this process reduces to a white noise sequence for $\tau_b = 0$, or an uncorrelated random walk for $\tau_b \to \infty$. The biases are additive and so the associated measurement sensitivity is simply

$$\boldsymbol{C}_b = \boldsymbol{I}_{2\times 2} \tag{21}$$

INITIAL RELATIVE ORBIT DETERMINATION

A proper consideration of the complete filtering procedure must begin with an initialization of the estimated state and state covariance. The presented initial relative orbit determination (IROD) method makes use of a batch of bearing angle measurements to estimate the initial ROE, with a minimum of three sets (six total data points) needed to reconstruct the six-dimensional state. The two-part algorithm is formulated to operate in arbitrarily eccentric J_2-perturbed orbits. First, an approximate unit vector of the initial ROE state is computed. Then, a solution for the unknown factor which appropriately scales that unit vector is sought using a second order expansion of the nonlinear measurement model.

Solving for the Initial ROE Unit Vector

Recall that Gaias et al.[3] present results indicating that the observability problem is largely decoupled and that the range ambiguity is well-captured by a single state element ($\delta\lambda$). This is further explored by Sullivan et al.,[5] where the IROD approach in that paper uses a reduced set of ROE that are scaled by $\delta\lambda$ to approximately capture the shape and orientation of the relative motion, but not the scale. Leveraging the intuition gained from these previous two works, this section is motivated by the fact that a unit vector should exist which accurately describes the shape and direction of the initial ROE, subject only to an unknown scaling factor.

Consider the nonlinear measurement model in Eq. (1). With some algebraic manipulation, it is possible to rearrange this exact model in a linear form with respect to the camera frame relative position, and thus with respect to the RTN frame relative position. The modified measurement model is given as

$$\boldsymbol{H}(\boldsymbol{y}(t))\boldsymbol{R}_{\mathcal{R}}^{\mathcal{C}}\delta\boldsymbol{r}^{\mathcal{R}}(t) = \boldsymbol{0}_{2\times 1} \tag{22}$$

where

$$\boldsymbol{H}(\boldsymbol{y}(t)) = \begin{bmatrix} c_\epsilon & 0 & -s_\epsilon \\ 0 & c_\alpha c_\epsilon & -s_\alpha \end{bmatrix}$$

Recall that, to first order, the RTN relative position can be written as

$$\delta\boldsymbol{r}^{\mathcal{R}}(t) = \frac{\partial\delta\boldsymbol{r}^{\mathcal{R}}}{\partial\delta\boldsymbol{x}_{\text{oe}}}\delta\boldsymbol{x}_{\text{oe}}(t) \tag{23}$$

Substituting the above equation into Eq. (22) and expressing the ROE state as a function of the initial conditions and the ROE STM yields

$$\widehat{\boldsymbol{H}}(t)\boldsymbol{\Phi}_{\text{oe}}(t,t_0)\delta\boldsymbol{x}_{\text{oe}}(t_0) = \boldsymbol{0}_{2\times 1} \tag{24}$$

where

$$\widehat{\boldsymbol{H}}(t) = \boldsymbol{H}(\boldsymbol{y}(t))\boldsymbol{R}_{\mathcal{R}}^{\mathcal{C}}\frac{\partial\delta\boldsymbol{r}^{\mathcal{R}}}{\partial\delta\boldsymbol{x}_{\text{oe}}}$$

With a batch of measurements taken at times t_1 through t_p, successive concatenations of Eq. (24) yields the following condition

$$\begin{bmatrix} \widehat{\boldsymbol{H}}(t_1)\boldsymbol{\Phi}_{\text{oe}}(t_1,t_0) \\ \widehat{\boldsymbol{H}}(t_2)\boldsymbol{\Phi}_{\text{oe}}(t_2,t_0) \\ \vdots \\ \widehat{\boldsymbol{H}}(t_p)\boldsymbol{\Phi}_{\text{oe}}(t_p,t_0) \end{bmatrix} \delta\boldsymbol{x}_{\text{oe}}(t_0) = \widehat{\boldsymbol{\mathcal{O}}}\delta\boldsymbol{x}_{\text{oe}}(t_0) = \mathbf{0}_{2p\times 1} \tag{25}$$

where the modified observability matrix, $\widehat{\boldsymbol{\mathcal{O}}}$, has been introduced. In the present formulation, it can be shown that this matrix is always full rank but poorly conditioned. Accordingly, $\widehat{\boldsymbol{\mathcal{O}}}$ has an empty null space and the only exact solution to Eq. (25) is the trivial $\delta\boldsymbol{x}_{\text{oe}}(t_0) = \mathbf{0}$. Instead, because $\widehat{\boldsymbol{\mathcal{O}}}$ is poorly conditioned (i.e., has a large ratio of maximum to minimum singular values), the approximate nontrivial null space can be determined by considering its singular value decomposition (SVD), $\widehat{\boldsymbol{\mathcal{O}}} = \boldsymbol{U}\boldsymbol{\Sigma}\boldsymbol{V}^{\text{T}}$. Looking at the modified observability matrix as a linear operator, the columns of $\boldsymbol{V}$ and $\boldsymbol{U}$ describe the input and output directions, respectively, which are scaled by the corresponding singular value entries on the diagonal of $\boldsymbol{\Sigma}$. It follows that the right singular vector associated with the minimum non-zero singular value, $\boldsymbol{v}_1$, approximates the null space of $\widehat{\boldsymbol{\mathcal{O}}}$ and thus provides an approximate initial ROE unit vector such that

$$\delta\boldsymbol{x}_{\text{oe}}(t_0) \approx c_1\boldsymbol{v}_1 \tag{26}$$

Here, c_1 is an unknown factor that scales the basis vector to the initial mean ROE state. The complete solution space is spanned by all of the column vectors of $\boldsymbol{V} = [\boldsymbol{v_1},\ \boldsymbol{v}_{2:6}]$, such that

$$\delta\boldsymbol{x}_{\text{oe}}(t_0) = c_1\boldsymbol{v}_1 + \boldsymbol{v}_{2:6}\boldsymbol{c}_{2:6} \tag{27}$$

where the remaining scaling factors, $\boldsymbol{c}_{2:6}$, are reasonably small compared to c_1.

At this stage, a novel closed-form analytical solution has been developed for determining the initial ROE state in eccentric J_2-perturbed orbits, subject only to an unknown set of scaling factors which can justifiably be reduced to a single unknown in accordance with Eq. (26).

Method for Determining the Unknown Scaling Factors

In the above solution for vector $\boldsymbol{v}_1$, a purely linear transformation is used to map from ROE to RTN frame relative position (i.e., Eq. 23). In doing so, Eq. (22) can be re-written as a linear system with respect to the initial ROE in order to arrive at the form of Eq. (27). However, retaining this linear transformation yields a system of homogeneous linear equations where the unknown scalars $[c_1,\ \boldsymbol{c}_{2:6}]^{\text{T}}$ can be factored out and thus remain ambiguous. Instead, if the transformation is captured to second order, Eq. (22) can be re-written as a system of homogeneous quadratic equations in terms of the unknown scaling factors, and a nontrivial solution can be obtained.

The complete nonlinear transformation from mean ROE to RTN positions is captured by the function $\boldsymbol{g}(\delta\boldsymbol{x}_{\text{oe}}(t), \boldsymbol{\text{oe}}_s(t))$ in Eq. (18). Expanding this function in a Taylor series about $\delta\boldsymbol{x}_{\text{oe}}(t) = \mathbf{0}$ yields to second-order

$$\begin{aligned} \delta r_j^{\mathcal{R}} \approx\ & g_j\Big|_{\substack{\mathbf{0} \\ \boldsymbol{\text{oe}}_s}} + \nabla g_j^{\text{T}}\Big|_{\substack{\mathbf{0} \\ \boldsymbol{\text{oe}}_s}} \boldsymbol{\Phi}_{\text{oe}}\delta\boldsymbol{x}_{\text{oe}}(t_0) + \dots \\ & + \frac{1}{2}\delta\boldsymbol{x}_{\text{oe}}(t_0)^{\text{T}}\boldsymbol{\Phi}_{\text{oe}}^{\text{T}}\nabla^2 g_j\Big|_{\substack{\mathbf{0} \\ \boldsymbol{\text{oe}}_s}} \boldsymbol{\Phi}_{\text{oe}}\delta\boldsymbol{x}_{\text{oe}}(t_0) \end{aligned} \tag{28}$$

where $\nabla g_j \in \mathbb{R}^6$ and $\nabla^2 g_j \in \mathbb{R}^{6\times 6}$ are the gradient and Hessian of g_j with respect to $\delta\boldsymbol{x}_{\text{oe}}(t)$, respectively, and the STM has been used to re-write the expansion in terms of the initial ROE state. Substituting Eq. (28) into the modified measurement model Eq. (22) and replacing the initial ROE state with the basis expansion

in Eq. (27) results in

$$\begin{aligned}\mathbf{0}_{2\times 1} =& \boldsymbol{H}\boldsymbol{R}_{\mathcal{R}}^{\mathcal{C}}\boldsymbol{g}\Big|_{\substack{\mathbf{0}\\ \boldsymbol{\text{oe}}_s}} + \boldsymbol{H}\boldsymbol{R}_{\mathcal{R}}^{\mathcal{C}}\nabla\boldsymbol{g}\Big|_{\substack{\mathbf{0}\\ \boldsymbol{\text{oe}}_s}} \boldsymbol{\Phi}_{\text{oe}}\left(c_1\boldsymbol{v}_1 + \boldsymbol{v}_{2:6}\boldsymbol{c}_{2:6}\right) + \dots \\ &+ \frac{1}{2}\boldsymbol{H}\boldsymbol{R}_{\mathcal{R}}^{\mathcal{C}}\begin{pmatrix}\left(c_1\boldsymbol{v}_1 + \boldsymbol{v}_{2:6}\boldsymbol{c}_{2:6}\right)^{\mathrm{T}}\boldsymbol{\Upsilon}_1\left(c_1\boldsymbol{v}_1 + \boldsymbol{v}_{2:6}\boldsymbol{c}_{2:6}\right)\\ \left(c_1\boldsymbol{v}_1 + \boldsymbol{v}_{2:6}\boldsymbol{c}_{2:6}\right)^{\mathrm{T}}\boldsymbol{\Upsilon}_2\left(c_1\boldsymbol{v}_1 + \boldsymbol{v}_{2:6}\boldsymbol{c}_{2:6}\right)\\ \left(c_1\boldsymbol{v}_1 + \boldsymbol{v}_{2:6}\boldsymbol{c}_{2:6}\right)^{\mathrm{T}}\boldsymbol{\Upsilon}_3\left(c_1\boldsymbol{v}_1 + \boldsymbol{v}_{2:6}\boldsymbol{c}_{2:6}\right)\end{pmatrix}\end{aligned} \tag{29}$$

with

$$\boldsymbol{\Upsilon}_j = \boldsymbol{\Phi}_{\text{oe}}(t,t_0)^{\mathrm{T}}\nabla^2 g_j\Big|_{\substack{\mathbf{0}\\ \boldsymbol{\text{oe}}_s}} \boldsymbol{\Phi}_{\text{oe}}(t,t_0)$$

For p measurement sets, evaluating Eq. (29) at each measurement time yields $2p$ quadratic equations in terms of the six unknown scaling factors $[c_1,\ \boldsymbol{c}_{2:6}]^{\mathrm{T}}$. Again as a bare minimum, three sets of bearing angles are needed. Potential solutions can be posed using nonlinear root-finding techniques such as the Newton-Raphson method, using nonlinear least-squares, or using quadratic optimization. Instead, this paper attempts to make some simplifying assumptions to reduce Eq. (29) to a linear form.

First, the relative RTN frame position components are nearly zero (neglecting osculating effects) when $\delta\boldsymbol{x}_{\text{oe}} = \mathbf{0}$, and thus $\boldsymbol{g}|_{\mathbf{0}} \approx \mathbf{0}$. Additionally, the terms containing $\boldsymbol{c}_{2:6}^{\mathrm{T}}(\cdot)\boldsymbol{c}_{2:6}$ can be neglected since they are reasonably smaller than all other terms. Furthermore, if all terms containing $\boldsymbol{c}_{2:6}$ are neglected, the following simplification is achieved

$$\mathbf{0}_{2\times 1} = c_1\boldsymbol{H}\boldsymbol{R}_{\mathcal{R}}^{\mathcal{C}}\nabla\boldsymbol{g}\Big|_{\substack{\mathbf{0}\\ \boldsymbol{\text{oe}}_s}} \boldsymbol{\Phi}_{\text{oe}}\boldsymbol{v}_1 + \frac{1}{2}c_1^2\boldsymbol{H}\boldsymbol{R}_{\mathcal{R}}^{\mathcal{C}}\boldsymbol{\Gamma} \tag{30}$$

with

$$\boldsymbol{\Gamma} = \begin{pmatrix}\boldsymbol{v}_1^{\mathrm{T}}\boldsymbol{\Upsilon}_1\boldsymbol{v}_1\\ \boldsymbol{v}_1^{\mathrm{T}}\boldsymbol{\Upsilon}_2\boldsymbol{v}_1\\ \boldsymbol{v}_1^{\mathrm{T}}\boldsymbol{\Upsilon}_3\boldsymbol{v}_1\end{pmatrix}$$

Notice that a power of c_1 can now be factored out. Evaluating the above at each measurement time results in $2p$ linear equations in one unknown (c_1) which can be solved via linear least-squares.

The scaling factor solution using this simplified method displays inconsistent behavior when validating using realistic measurements simulated in high-fidelity. This is likely due to neglecting terms that are first-order in the dominant scaling factor c_1 in order to achieve a form amenable to linear least-squares. Accordingly, the original quadratic equations in Eq. (29) must be reconsidered in future research efforts. A temporary alternative method to obtaining the scaling factor is presented in the following.

Obtaining the Scaling Factor from Coarse A Priori Information

At this stage, it is necessary to obtain the unknown scaling factor from a priori information available to the servicer spacecraft. In general, this information will be a coarse measurement of the relative separation magnitude between the servicer and target, which can be obtained either through the use of NORAD TLE or from a designated radar campaign. Conservatively, range errors on the order of at least 10% are expected. The IROD method implemented hereafter solves for the unit vector using the previously established solution and then scales the estimated unit vector by the coarse relative range measurement provided.

To test the overall functionality of this approach, a Monte Carlo simulation is conducted which assumes that the initial ROE is sampled from a representative multivariate Gaussian distribution and the relative range measurement is made available to the servicer with an assumed 15% error. The measurements provided to the IROD algorithm are generated using the high-fidelity numerical propagation capability that will be employed in the subsequent filter validation. Table 1 provides the noise parameters assumed for the camera sensor, as well as for the servicer absolute position, velocity, and attitude knowledge. The servicer absolute orbit initial

Table 1: Sensor noise parameters used in high-fidelity simulation.

Measurement Noise			Servicer Knowledge Noise			
$\sigma_{\alpha/\epsilon}$	$\sigma_{b,\alpha}$	$\sigma_{b,\epsilon}$	σ_{pos}	σ_{vel}	$\sigma_{\text{att, off-axis}}$	$\sigma_{\text{att, roll}}$
18”	5”	5”	50 m	0.50 m/s	6”	40”

conditions are the same as in Table 2. Note that r_p denotes the servicer perigee radius. The multivariate Gaussian mean and standard deviation values for sampling the initial relative state are

$$\delta\bar{\boldsymbol{x}}_{\text{oe}}(t_0) = \begin{pmatrix} -50 & -12000 & 300 & 100 & -300 & 100 \end{pmatrix}^{\text{T}} \text{m} \tag{31}$$

$$\sigma_{\delta\boldsymbol{x}_{\text{oe}}(t_0)} = \begin{pmatrix} 25 & 5000 & 100 & 100 & 100 & 100 \end{pmatrix}^{\text{T}} \text{m} \tag{32}$$

The initial relative orbit geometries are characterized by large mean along-track separations as indicated by large relative mean longitude terms. Accordingly, it is expected that the majority of the relative range error (in these cases, at the kilometer level) is absorbed by $\delta\lambda$ whereas the remaining five ROE should be strongly observable and estimated to good accuracy. This is consistent with the intuition that the observability problems are largely confined to the relative mean longitude, and that the other parameters accurately describe the shape and orientation of the relative motion. The Monte Carlo simulation consists of 250 runs, wherein the initial ROE is sampled once per run and the number of measurements used in the IROD algorithm is varied from five to sixty. Measurements are provided at 30 second intervals. The results of this simulation are shown in Figures 3 and 4 and Table 5 in the Appendix, where the initial ROE estimation error is given as a function of the number of measurement sets used for each of the 250 runs.

As expected, the majority of the scaling factor error is largely absorbed by the $\delta\lambda$ estimate, as seen by constant bands of estimation error in the upper right subplot. Instead, the remaining five parameters converge to favorable estimates for all simulation runs. Notably, the relative semi-major axis and relative eccentricity components generally converge with a drastic decrease in the sample standard deviation after a large transient error phase of approximately twenty-five measurements, whereas the relative inclination components are immediately quite accurate using five measurements and do not improve drastically with more measurements. The Monte Carlo sample mean ($\bar{\mu}$) and standard deviation (σ) statistics when using ten, thirty, and sixty measurements are provided in Table 5. The IROD capability tested here represents a distinct improvement over the approach in[5] since it is generalized to J_2-perturbed orbits of arbitrary eccentricity and requires substantially less measurement time to obtain more accurate results. Furthermore, this new method largely confines initialization error from coarse relative range information to a single component of the ROE vector ($\delta\lambda$). This is a powerful advantage over the methods implemented in the ARGON[6] and AVANTI[7] demonstrations, where the erroneous a priori relative position and velocity information from TLE or radar campaigns is mapped into each element of the ROE state. From a space situational awareness perspective, this new method demonstrates the potential to improve initial coarse orbit products by using sparse imaging from a spacecraft in orbit.

MANEUVER-FREE FILTER DESIGN AND VALIDATION

At this stage, the necessary dynamical system framework has been established and the method for filter initialization has been formulated and tested. The following sections highlight the design and validation of multiple navigation filters which are better suited to handle the generally weak observability and corresponding numerical sensitivity associated with angles-only navigation. Unlike several previous approaches in angles-only navigation, the filters presented here are able to operate without the need for maneuvers dedicated to observability improvement. As a motivation, consider that such a filter architecture effectively decouples the navigation and maneuver-planning processes and enables more fuel-efficient rendezvous by removing the need for frequent observability maneuvers. The original context for the maneuver-free angles-only filter comes from Sullivan et al.,[5] where an EKF-based approach was successful in reconstructing the full ROE state particularly when the relative motion was drifting due to a difference in semi-major axis between the

Table 2: Servicer absolute orbit and relative orbit test cases.

Servicer œ	r_p [km]	e [-]	i [°]	Ω [°]	ω [°]	M_0 [°]
	7200	0.5	30	60	120	180
	Relative Orbital Elements [m]					
Test Case	$a\delta a$	$a\delta\lambda$	$a\delta e_x$	$a\delta e_y$	$a\delta i_x$	$a\delta i_y$
RO1	0	-30000	500	0	-500	0
RO2	-150	-20000	300	0	-300	0
RO3	0	-5000	0	0	0	0

two spacecraft. However, that work is confined to strictly near-circular orbits and demonstrated several deficiencies in the filter functionality, including sensitivity to filter tuning parameters, slow convergence rates (approximately ten orbits to converge to reasonable estimates), and inconsistent estimation for several important near-circular orbital geometries including co-orbital leader-follower configurations, as well as far- to mid-range hold point configurations of equal energy (i.e., $\delta a = 0$). Accordingly, this paper addresses these shortcomings by systematically formulating filter variants which are able to estimate useful parameters that aid in improved convergence speed, consistency, and robustness for relevant orbital geometries without pursuing excessively complex implementations.

The filter designs are assessed for three nominal relative orbit (RO) scenarios which emulate phases of a rendezvous operation. Table 2 provides the servicer absolute orbit initial conditions and initial mean ROE test cases describing each of the relative orbit trajectories. RO1 is representative of a far-range hold point and RO2 introduces a small difference in semi-major axis, which enables the servicer to approach the target on a naturally drifting relative trajectory. RO3 describes a leader-follower type of configuration marked by pure along-track separation with no oscillations in the radial or cross-track directions.

For each test case, the position and velocity of the servicer and target are numerically propagated using rigorous full-force models, including the GRACE GGM01S gravity model of order and degree 120, a Harris-Priester atmospheric drag model, third-body sun and moon gravity, and solar radiation pressure with a cylindrical Earth shadow model. For an in-depth discussion of this simulation tool, the work by Eddy et al.[26] is recommended. This simulated truth trajectory is then used to generate simulated bearing angles and Global Positioning System (GPS) Position/Velocity/Time (PVT) solutions that are augmented with additive noise. Recall, Table 1 shows the noise statistics for the bearing angle measurements and biases, as well as the servicer's orbit and attitude knowledge. The bearing angle and attitude knowledge noise parameters are consistent with the Blue Canyon Technologies star tracker and attitude determination system,[27] and the GPS noise parameters are consistent with the achievable solution accuracy using weak signal tracking in elliptical orbits (see NASA's Magnetospheric MultiScale Mission navigation performance[28]). Finally, the numerically propagated position and velocity of the servicer and target are transformed to corresponding osculating orbital element sets (see Schaub and Junkins [23, ch. 9]) and then numerically averaged to produce the mean elements subject to the above perturbations. Finally, the reference truth ROE are assembled from the numerically computed mean elements according to Eq. (2). All estimation errors are calculated by differencing the output mean ROE of the estimation algorithm from the numerical truth ROE set.

The EKF is considered as the baseline filter architecture to estimate the ROE state, both for its ubiquity in space navigation applications and to maintain consistency with previous works (see[5,7]). As previously mentioned, the nonlinear dynamics and/or measurement models are accommodated in the EKF by performing a linear Taylor series expansion at each estimation step. While the EKF allows for direct application of the nonlinear dynamics model in the estimate time-update (or *prediction*) step, the previously established STM solution is adopted for its ease of implementation, and to avoid computationally expensive numerical integration within the filter. Instead, the nonlinear measurement model in Eq. (1) is retained for the

measurement-update (or *correction*) step and the associated linearization in Eq. (11) is only used to compute the Kalman gain and state covariance update. Alternatively, the strategic choice to implement the UKF is largely founded in its ability to retain the nonlinear measurement model through all phases of the filtering procedure at practically no extra cost in computational complexity. As previously discussed, accounting for nonlinear modeling characteristics (particularly those related to osculating effects) improves the filters ability to map separation-dependent variations in the measured bearing angles to ROE variations which capture range information. The UKF forgoes linearizing the measurement model Taylor series by implementing a stochastic weighted regression procedure. As an improvement to handle dynamics modeling deficiencies, adaptive forms of the EKF and UKF are formulated to estimate the process noise statistics online in a targeted effort to improve filter stability and performance over a variety of orbit scenarios.

Adaptive Noise-Tuning Filters

The selection of Kalman filter process and measurement noise statistics is of interest since it is known that these features can largely influence the filter stability and performance, particularly for nonlinear variants like the EKF and UKF. Process noise is generally included to account for dynamics that are unmodeled by the filter, and to aid in stability by increasing the updated state covariance which keeps the filter receptive to new measurements. The measurement noise statistics are implemented to account for sensor mismodeling in the filter, and can often be accurately determined by hardware testing. The intent of this section is to develop a mathematical framework for a class of adaptive nonlinear filters which are able to tune the process and/or measurement noise statistics online. This design consideration is founded on the strategy that more accurately accounting for the dynamical processes through an adaptive method can help overcome observability issues related to mismodeling and linearization, and thus mitigate numerical sensitivity and inconsistent filter performances.

Adaptive filtering frameworks have been established in several previous research studies. Most notably, Mehra[29,30] develops the mathematical foundation for four main categories of adaptive filtering methodologies, namely the Bayesian, maximum likelihood, correlation matching, and covariance matching techniques. Meyers and Tapley[31] further expand upon the covariance matching technique, and discuss numerical results in the context of ground-based tracking of LEO satellites. Other research applications for adaptive estimation have been explored in terrestrial target tracking by Maybeck et al.,[32] spacecraft attitude determination by Mehra et al.,[33] and in spacecraft relative navigation using carrier-phase differential GPS by Busse et al.[34] In the following, an adaptive approach is designed for angles-only relative navigation using the innovation covariance matching technique.

In Kalman filtering, the term *innovation* is generally used to describe the residual formed by the difference between a measurement received by the filter and the expected measurement conditioned on the current state estimate. Alternatively, the term *pre-fit residual* is commonly used in spacecraft orbit determination. This quantity is given by

$$\Delta_k^y = \boldsymbol{y}_k - \boldsymbol{h}(\hat{\boldsymbol{x}}_{k|k-1}) \approx \boldsymbol{y}_k - \boldsymbol{C}_k \hat{\boldsymbol{x}}_{k|k-1} \tag{33}$$

where Δ_k^y denotes the measurement innovation at timestep k. Note that $\hat{\boldsymbol{x}}_{i|j}$ denotes the state estimate at time step t_i using measurements up to and including time step t_j. Thus, $\hat{\boldsymbol{x}}_{k|k-1}$ represents the a priori (time-updated) state estimate and $\hat{\boldsymbol{x}}_{k|k}$ represents the subsequent a posteriori (measurement-updated) estimate at time step t_k. The fundamental idea in innovation covariance matching is to use the statistics of a sample of innovations, in conjunction with their theoretical values, to infer the quantities being adaptively tuned in the filter. To that end, Sullivan and D'Amico[22] derive the following relationship relating the theoretical covariance of the measurement innovation $\left(\boldsymbol{\Sigma}_{\Delta_k^y}\right)$ to the sample covariance $\left(\widehat{\boldsymbol{\Sigma}}_{\Delta_k^y}\right)$ of a set of N measurement innovations collected in a sliding window

$$\boldsymbol{\Sigma}_{\Delta_k^y} = \boldsymbol{C}_k \hat{\boldsymbol{P}}_{k|k-1} \boldsymbol{C}_k^{\mathrm{T}} + \boldsymbol{R}_k \approx \widehat{\boldsymbol{\Sigma}}_{\Delta_k^y} = \frac{1}{N} \sum_{i=k-N+1}^{k} \Delta_i^y \Delta_i^{y^{\mathrm{T}}} \tag{34}$$

The above equation can be used to immediately estimate the measurement noise covariance matrix, $\boldsymbol{R}_k$, from a sequence of measurement innovations. For this paper, it is assumed that the sensors are well-modeled and

the measurement noise statistics are known accurately enough to not require online estimation. Accordingly, the above approach is augmented to map measurement innovations to corresponding state innovations via the Kalman gain in order to estimate the process noise covariance. Again, this is explored and fully derived by Sullivan and D'Amico[22] and given as

$$\boldsymbol{Q}_k \approx \boldsymbol{\mathcal{K}}_k \widehat{\boldsymbol{\Sigma}}_{\Delta_k^y} \boldsymbol{\mathcal{K}}_k^{\mathrm{T}} \tag{35}$$

where $\widehat{\boldsymbol{\Sigma}}_{\Delta_k^y}$ is highlighted in Eq. (34).

As a final note, the estimate of $\boldsymbol{Q}_k$ must abide by the general structure of a covariance matrix. That is, the estimate must be properly adjusted to be symmetric positive semi-definite. Accordingly, a procedure inspired by the work of Higham[35] is applied in which the nearest symmetric positive semi-definite matrix is obtained through a spectral decomposition of the matrix computed in Eq. (35). In this context, "nearest" indicates that the Frobenius norm of difference between the original and the adjusted covariance matrix is minimized. For further improvement of the numerical stability, a regularization procedure is implemented such that the adjusted process noise covariance matrix estimate does not change substantially over one filtering iteration. This is achieved by placing the following constraint

$$\max \text{ eig}\left(\boldsymbol{Q}_k\right) \leq \Lambda \cdot \max \text{ eig}\left(\boldsymbol{Q}_{k-1}\right) \tag{36}$$

where the function eig $(\cdot)$ returns the eigenvalues of the matrix in the argument, and Λ is a regularization factor that controls the allowable relative growth of the covariance estimate based on the maximum eigenvalue.

Numerical Results

The four filtering strategies (EKF, UKF, and their respective adaptive variants) are now implemented and validated for estimating the relative motion ROE state and the bearing angle biases. The initial ROE estimates and covariances are provided by IROD, and the initial bearing angle biases are initialized to zero with an initial standard deviation of 100". Measurements are sparsely received at 300s intervals, and once again the measurement noise covariance is assumed to be 25". The true bearing angle biases are set to a constant 100", and τ_b is chosen as ∞ to model the biases as random walk processes. Finally, the sliding window size N and regularization factor Λ used by the adaptive routines are set to 10 and 3, respectively. To evaluate filter convergence and performance, the estimation error statistics (mean and standard deviation) for each filter test are computed over the last four simulated orbits and tabulated in Table 3 and Table 4. As previously discussed in this paper, and highlighted in other works (see[3,5]), the observability issues are largely confined to estimating the relative mean longitude, $a\delta\lambda$. Accordingly, the estimation error and 1-σ filter formal standard deviation of this state element is provided in the Appendix (see Figures 5-7) for each simulation. Note that the estimation error of all other ROE scales with the error in the relative mean longitude.

The discussion begins with the RO1 configuration, which does not contain a difference in semi-major axis between the target and servicer. Since the angles-only navigation problem is intrinsically observability-constrained when not implementing maneuvers, the relative drift induced by a nonzero semi-major axis difference creates a favorable natural variation in the relative motion that acts similar to a maneuver profile. Accordingly, EKF convergence tends to be more consistent with such geometries and, conversely, tends to be less consistent when the orbits are of equal energy (i.e., $a\delta a = 0$). This latter condition is demonstrated in Figure 5a, where the EKF and A-EKF estimates of $a\delta\lambda$ diverges over the simulation period. The data in Table 3 and the full-state estimation trends in Figure 8 confirm that the nonzero ROE components ($a\delta e_x$ and $a\delta i_x$) are also estimated poorly (errors on the order of 100 m and 60 m, respectively, from the EKF and A-EKF) since their error effectively scales with the relative mean longitude error. Instead, both the UKF and A-UKF show distinct convergent trends for the RO1 geometry (see Figure 5b and Figure 9), with the A-UKF outperforming in both convergence speed and accuracy. Over the last four orbits, the UKF settles to an estimate that is approximately 3% of the true relative mean longitude (error of 566 ± 160), but still maintains accurate estimation of the other ROE parameters within approximately 2%. The A-UKF instead estimates the relative mean longitude to within 148 ± 106 m, which represents a worst-case error that is less than 1% of the true value. Furthermore, the nonzero ROE components are estimated to within 5 m (1%) of their true value while the other components are estimated with sub-meter level accuracy. These latter results

Table 3: Filter ROE estimation error statistics computed over last four orbits of simulation.

		ROE estimation error, $\bar{\mu} \pm \sigma$ [m]					
Filter	RO	$a\delta a$	$a\delta\lambda$	$a\delta e_x$	$a\delta e_y$	$a\delta i_x$	$a\delta i_y$
EKF	1	2.2 ± 1.5	-6161.0 ± 954.9	104.4 ± 16.5	1.3 ± 1.0	-102.4 ± 16.0	1.1 ± 0.6
	2	-1.8±2.3	130.5 ±85.1	-7.2 ±3.5	3.3 ±1.0	5.1 ±3.8	-0.2 ±1.1
	3	0.2±0.2	-2026.0 ±243.3	-0.1 ±0.1	0.7±0.1	0.0 ±0.0	0.0±0.0
A-EKF	1	0.7±1.0	-3750.0±430.9	61.9 ± 7.0	2.3 ± 0.6	-62.1±7.1	0.4 ± 0.3
	2	2.9±2.4	150.3±113.3	-5.8±4.4	-0.1±0.3	6.0±4.6	0.1 ±0.3
	3	0.5±0.2	-2319.3 ±264.9	0.2 ±0.2	0.4 ±0.2	0.0 ± 0.1	0.0 ±0.1
UKF	1	1.6±1.1	566.1±158.5	-8.6 ± 2.7	-1.6 ± 1.0	9.9 ± 2.7	-0.1±0.7
	2	-3.1 ±2.0	57.1±90.4	-2.5 ±3.0	2.6 ±0.8	0.7 ±3.2	-0.3 ±1.1
	3	-2.2±0.4	-525.5±84.7	-1.5 ±0.5	1.7±0.4	0.0 ±1.0	-0.6 ± 0.9
A-UKF	1	0.1±1.0	147.7 ±105.8	-4.2±3.5	-0.1 ±0.7	4.1 ±3.5	-0.2±0.5
	2	-0.9 ±0.9	-38.3 ± 48.6	1.4 ± 1.85	0.2±0.3	-1.4 ±1.9	-0.1 ±0.2
	3	-0.2±0.3	14.3±29.9	-0.1 ±0.1	0.3 ±0.1	0.0 ±0.1	0.0± 0.1

Table 4: Filter bias estimation error statistics computed over last four orbits of simulation.

		Bias estimation error, $\bar{\mu} \pm \sigma$ [arcsec]	
Filter	RO	b_α	b_ϵ
EKF	1	2.84 ± 0.25	19.03 ±7.01
	2	7.32 ±0.19	107.36 ±2.35
	3	3.15 ± 0.27	27.26 ±2.98
A-EKF	1	2.64±0.27	10.22 ±1.30
	2	2.68 ± 0.17	2.07 ±3.12
	3	3.09 ±0.23	7.55±4.21
UKF	1	2.93 ±0.24	-16.88±4.02
	2	7.97 ±0.21	84.28± 0.80
	3	23.35 ±2.84	32.30 ± 7.11
A-UKF	1	2.31± 0.18	-2.62±1.11
	2	2.41 ±0.19	3.72 ± 1.35
	3	3.60 ±0.25	9.25 ±3.35

are a strong indication that the strategic inclusion of a fully nonlinear measurement model in the UKF provides the necessary improvements to overcome the numerical observability constraints ailing the EKF-based filters, while the adaptive process noise tuning serves the intended purpose of improving filter performance and convergence speed by supplementing the linear dynamics model within the filter.

With regard to the estimation of azimuth and elevation angle biases in RO1, it is first noteworthy to mention that all filters converge effectively to an accurate estimate of the azimuth bias that is within approximately 3 arcsec of the true value. Recall from Figure 1 that the azimuth describes relative motion variation in the cross-track direction, which is not characterized by any mean offsets according to the developed dynamics model. Accordingly, any measurement bias in the azimuth is quickly picked up by the filter. Instead, the elevation angle (which largely captures in-plane relative motion variations) is evidently harder to estimate quickly and accurately. Both Sullivan et al.[5] and D'Amico et al.[6] highlight an expected bias in the elevation angle that occurs from offsets due to the natural curvature of the orbit. This bias is more pronounced with larger along-track separations. As such, it is generally more difficult for the filter to resolve the overall elevation

bias resulting from large along-track separations and intrinsic sensor flaws using a linearized measurement sensitivity model (as in the EKF) that does not fully account for the curvature effect. While the EKF, A-EKF, and A-UKF estimate the elevation bias to within approximately 20 arcsec over the last four simulated orbits, only the A-UKF is able to effectively estimation accuracy that is comparable to the azimuth bias results (approximately 4 arcsec). The estimation error trends and 1-σ bounds of the elevation bias are shown in Figure 10 for RO1.

The ROE estimation results for RO2 are shown in Figure 6 and largely confirm the conclusion from Sullivan et al.[5] that a difference in semi-major axis produces a sufficient amount of long-term variation in the relative motion to achieve reasonable filter convergence. This is evidenced by the ability of the EKF and A-EKF (see Figure 6a) to estimate $a\delta\lambda$ to within 130 ± 85 and 150 ± 113 m, respectively, over the last four simulated orbits. Note from the figures that the inclusion of adaptive process noise tuning effectively decreases the necessary time to convergence by approximately four orbits. The UKF-based results show even better convergence accuracy, with the UKF estimating the relative mean longitude to within 57 ± 90 m and the A-UKF estimating to within 38 ± 49 m. Note that the adaptive process noise tuning for the A-UKF improves both filter convergence speed (see Figure 6b) and steady-state standard deviation of the estimate. As expected, all filters achieve good estimation accuracy of the azimuth bias, with the adaptive filters outperforming their standard counterparts by approximately 5 arcsec. For the elevation bias, Figures 11a and 11b indicate that EKF and UKF struggle to arrive at accurate estimates (errors of 107 ± 2 and 84 ± 1 arcsec, respectively). As before, the adaptive filters instead enable the elevation bias to be captured more effectively, with errors of 2 ± 3 and 4 ± 1 arcsec for the A-EKF and A-UKF, respectively. The insight here is that the filter is able to pick up the bearing angle biases more effectively since the process noise model is being adaptively improved, which leads to a better correlation between the observed bearing angle trends and the propagated ROE within the filter.

Finally, the estimation of the RO3 geometry is simulated and the ROE error trends are provided in Figure 7 followed by the elevation bias trends in Figure 12. Note that this geometry is marked by only pure along-track separation, where the target appears very nearly constant in the image frame. The only variations in the relative motion that the filter can rely upon to reconstruct the relative range are due to the differential perturbation effects which cause slight oscillations in the bearing angles on the order of a few hundred arcseconds. Accordingly, without a highly accurate measurement model, the observability issues are irreconcilable and the estimate is likely to diverge. This is behavior is evident in the performance of the EKF and A-EKF (see Figure 7a) where the relative mean longitude estimate diverges over time. Even though $a\delta\lambda$ is diverging, Table 3 shows that the filters are able to estimate all other components of the ROE vector to high accuracy. This is again largely because the unobservability is confined to the relative mean longitude, and thus, the filter is able to definitively determine the shape of the relative motion (i.e., all nonzero ROE errors should scale with the relative mean longitude knowledge). Once again, where the EKF-based approaches fail to converge to stable and accurate estimates, the UKF-based approaches succeed (see Figure 7b). In the RO3 case, the UKF displays a clear, yet slow convergent phase. Over the last four orbits, it achieves an estimation error of 525 ± 85 m, which is still substantial but markedly improved over the EKF and A-EKF results. Instead, the A-UKF estimates $a\delta\lambda$ to within 14 ± 30 m, which represents a worst-case error that is just under 1% of the true value. As in the previous cases, the adaptive filters are better able to estimate the elevation bias with good accuracy as compared to the standard filter variants. The A-EKF and A-UKF respectively achieve errors of 8 ± 4 arcsec and 9 ± 3 arcsec, which offer a substantial improvement over the EKF and UKF errors on the order of 30 arcsec.

Overall, there are several definitive and critical trends in the estimation results presented here. First, in the cases where the bearing angles are only varying due to subtle oscillations imposed by the differential osculating perturbation effects in orbits of equal energy (i.e., $\delta a = 0$), the EKF-based approaches simply fail. It stands to reason that the necessary linearization of the measurement model effectively precludes a proper mapping of observed bearing angle trends to a correspondingly accurate estimate of the relative motion trends that properly rectifies the relative separation. This fact is seen clearly in the full-state estimation errors and 1-σ bounds for the RO1 configuration shown in Figure 8. Instead, the UKF-based approaches display distinct stability and convergence phases in all relative motion configurations. See Figure 9 for an example of the full

ROE state estimation errors and 1-σ bounds for the RO1 configuration. These results are a strong testament to the importance of retaining nonlinear effects (particularly those separation-dependent effects related to the mean-to-osculating transformation) in the measurement model. Furthermore, the inclusion of adaptive process noise tuning has definitively served the purpose of improving convergence accuracy and speed for all instances where the standard counterpart is already stable, but slower to converge. While the A-EKF models in RO1 and RO3 still show divergence, it is evident that the process noise tuning is attempting to correct for this but cannot overcome the limitations imposed by the measurement model linearization. Finally, the A-UKF outperforms all other filtering strategies when considering the ROE estimation accuracy, speed, stability (as evidenced by error standard deviation) and robustness (as evidenced by consistent estimation in all geometries), as well as the effective estimation of the sensor bearing angle biases. This estimator consistently delivers errors of the relative mean longitude (and thus, the relative range) that are within 1% of the true value, while also estimating the remaining ROE at meter and sub-meter levels throughout.

CONCLUSIONS

This research has addressed the problem of developing filter algorithms which do not require maneuvering to estimate the relative orbital motion of a target space object with respect to an observing spacecraft in eccentric orbits using only bearing angles received by the servicer onboard camera. As part of the estimation architecture development, the problem of angles-only initial relative orbit determination was addressed to provide an initialization to the sequential navigation filter. Unlike other approaches which constrain the initial relative orbit determination problem to circular unperturbed orbits, the method in this paper was formulated for implementation in eccentric J_2-perturbed orbits. While the approach was shown to accurately capture the unit vector associated with the initial relative orbital element state, the solution for the necessary scaling factor to complete the unique initialization suffered from the simplifying assumptions used to attempt a linear least-squares solution. Still, the definitive advantages of the new solution procedure were evidenced by the consistent initialization accuracy for a multitude of relative motion geometries while requiring less total measurement time and only relying on coarse relative range knowledge with kilometer-level error.

With regard to the sequential estimation architectures developed in this work, several key lessons were learned. First, in assessing the ability of the extended Kalman filter (EKF) to estimate the relative orbital element state, inconsistent performance for several relative motion scenarios provided a strong indication that the dynamics and measurement model linearizations required by the EKF substantially limit the achievable observability, and thus, filter consistency and accuracy. Accordingly, an adaptive variant of the EKF which tunes the process noise statistics online was developed and validated. Instead, by leveraging the ability to forgo measurement model linearization while retaining the simplicity of linear dynamics in the unscented Kalman filter (UKF) framework, the filter performance showed distinct stability and performance advantages in cases where there was not large variation of the relative motion due to a nonzero difference in semi-major axis. This is largely due to UKF ability to accurately correlate nonlinear, separation-dependent osculating effects observed in the bearing angle measurements to correspondingly improved separation-rectified variations in the relative motion. However, it is noted that even though the UKF presented clearly distinct convergence benefit as compared to the EKF-based architectures, convergence occurs slowly (particularly in the difficult-to-observe pure along-track separation RO3 case). Thus, the strategic choice was made to supplement the linearized dynamics model with adaptive process noise tuning. This adaptive UKF outperformed every other variant across the board (including in the particularly difficult pure along-track case), estimating the ROE state and sensor biases to higher accuracy with faster convergence than previous designs, and with formal covariances that accurately reflected the true error trends. The results conclusively argue for the fact that, by combining a fully nonlinear measurement model with improvements to the process model through adaptive tuning, the novel application of the adaptive UKF to angles-only navigation enables consistent maneuver-free estimation in eccentric orbits subject to realistic simulation testing.

APPENDIX

Initial Relative Orbit Determination (IROD) Monte Carlo Simulation Results

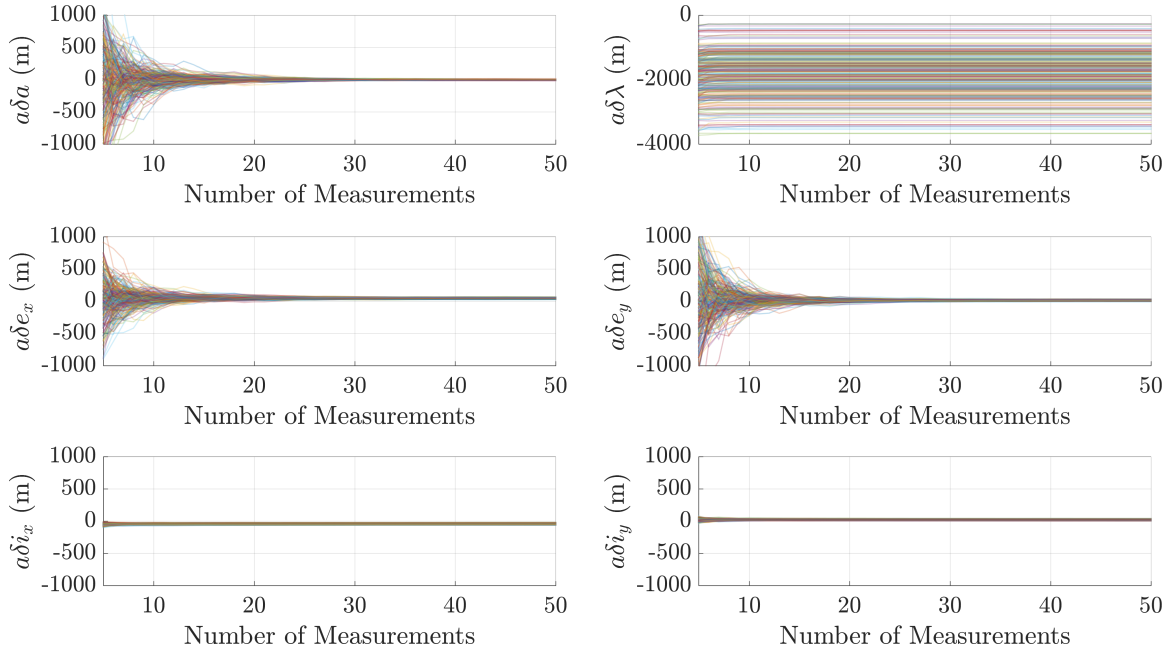

Figure 3: IROD error from 250 Monte Carlo simulations assuming 15% error in range knowledge.

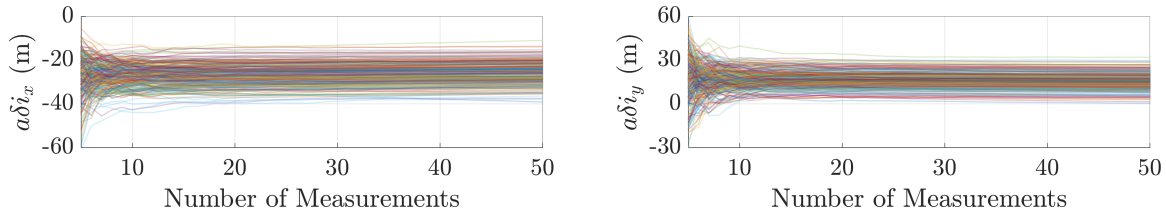

Figure 4: Zoomed in view showing δi error trends and convergence.

Table 5: IROD Monte Carlo performance sample statistics

#	$a\delta a$ [m]		$a\delta e_x$ [m]		$a\delta e_y$ [m]		$a\delta i_x$ [m]		$a\delta i_y$ [m]	
meas.	$\bar{\mu}$	σ	$\bar{\mu}$	σ	$\bar{\mu}$	σ	$\bar{\mu}$	σ	$\bar{\mu}$	σ
10	75.1	97.6	50.2	58.1	61.5	79.2	29.0	7.3	16.2	6.2
30	2.4	3.0	29.2	6.2	6.3	5.6	27.4	7.0	14.7	5.1
60	2.1	2.3	27.9	5.6	6.6	5.3	26.1	7.0	14.0	5.0

Filter Simulation ROE Results

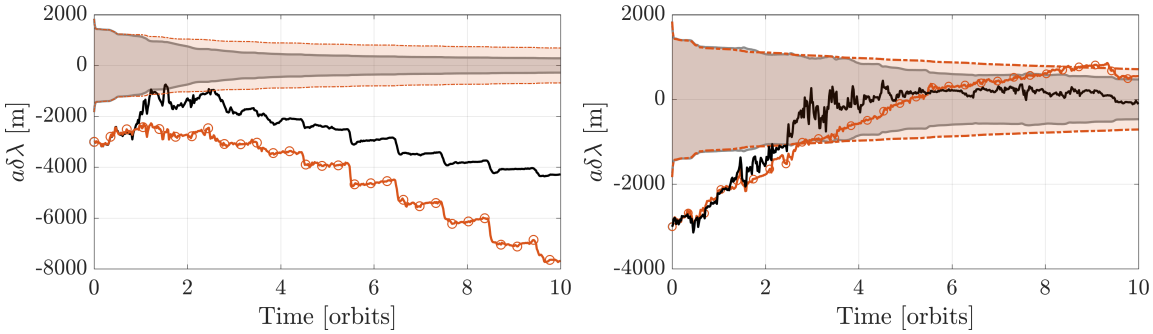

(a) EKF and A-EKF estimation error and 1-σ bounds. (b) UKF and A-UKF estimation error and 1-σ bounds.

Figure 5: $a\delta\lambda$ estimation error for RO1 using standard (dashed/circles) and adaptive (solid) Kalman filters.

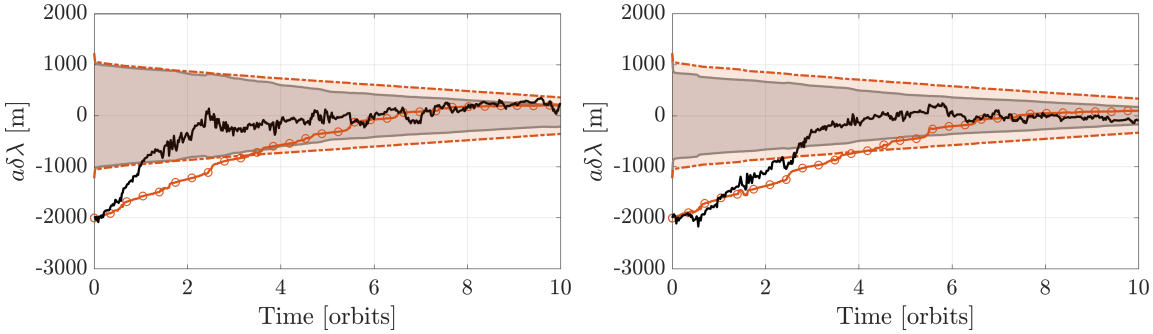

(a) EKF and A-EKF estimation error and 1-σ bounds. (b) UKF and A-UKF estimation error and 1-σ bounds.

Figure 6: $a\delta\lambda$ estimation error for RO2 using standard (dashed/circles) and adaptive (solid) Kalman filters.

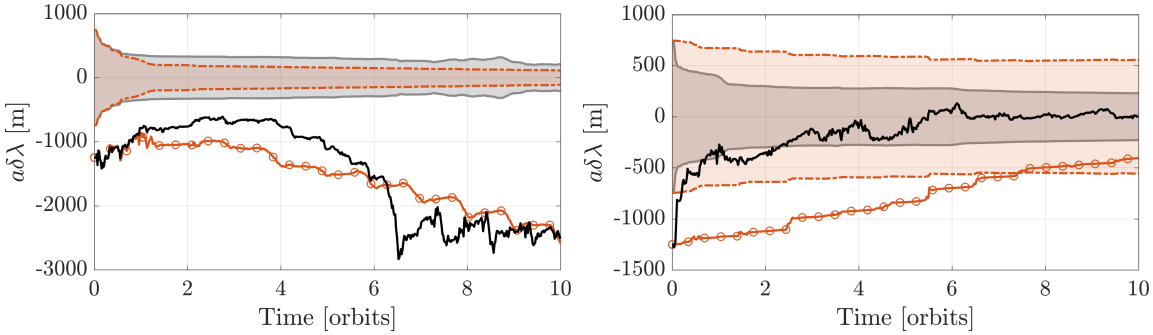

(a) EKF and A-EKF estimation error and 1-σ bounds. (b) UKF and A-UKF estimation error and 1-σ bounds.

Figure 7: $a\delta\lambda$ estimation error for RO3 using standard (dashed/circles) and adaptive (solid) Kalman filters.

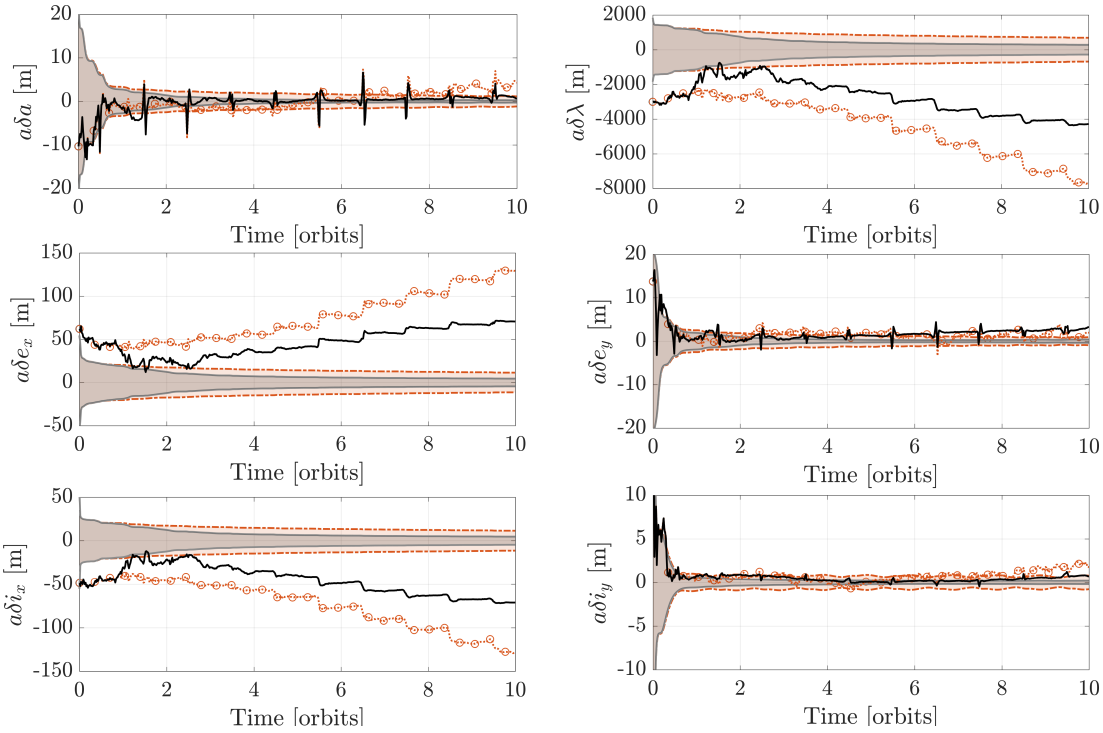

Figure 8: Estimation for RO1 using EKF (dashed/circles) and adaptive EKF (solid)

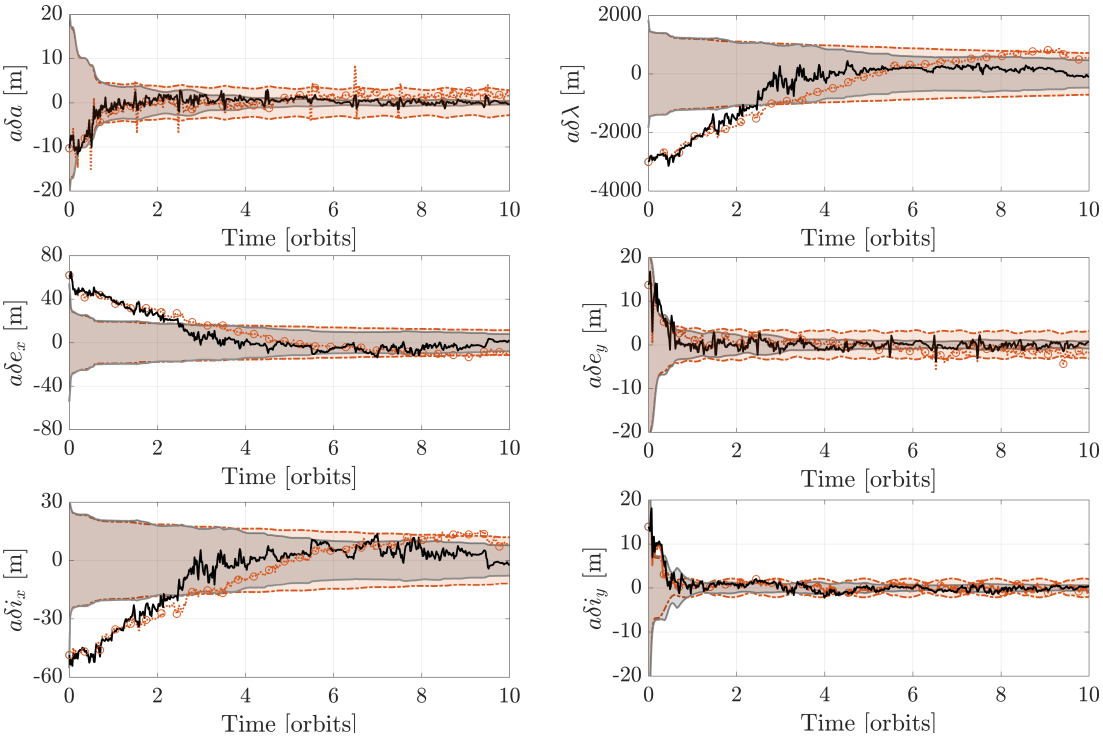

Figure 9: Estimation for RO1 using UKF (dashed/circles) and adaptive UKF (solid)

Filter Simulation Elevation Bias Results

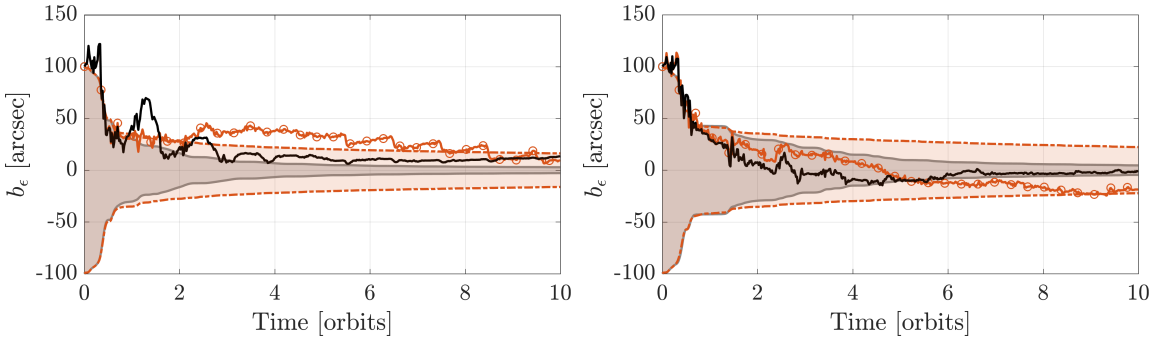

(a) EKF and A-EKF estimation error and 1-σ bounds.

(b) UKF and A-UKF estimation error and 1-σ bounds.

Figure 10: b_ϵ estimation error for RO1 using standard (dashed/circles) and adaptive (solid) Kalman filters.

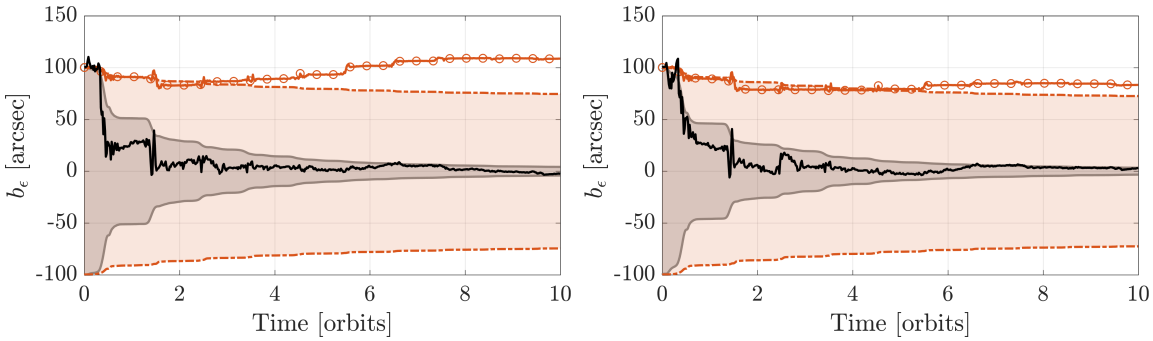

(a) EKF and A-EKF estimation error and 1-σ bounds.

(b) UKF and A-UKF estimation error and 1-σ bounds.

Figure 11: b_ϵ estimation error for RO2 using standard (dashed/circles) and adaptive (solid) Kalman filters.

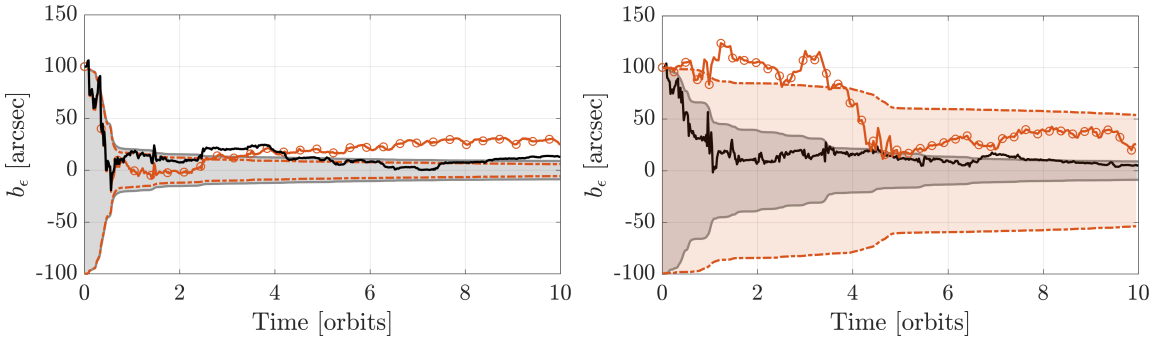

(a) EKF and A-EKF estimation error and 1-σ bounds.

(b) UKF and A-UKF estimation error and 1-σ bounds.

Figure 12: b_ϵ estimation error for RO3 using standard (dashed/circles) and adaptive (solid) Kalman filters.

ACKNOWLEDGMENTS

This work was supported as part of the Air Force Research Laboratory's Control, Navigation, and Guidance for Autonomous Spacecraft (CoNGAS) project under contract FA9453-16-C-0029. The authors are thankful for their support.

REFERENCES

[1] S. D'Amico, M. Pavone, S. Saraf, A. Alhussien, T. Al-Saud, S. Buchman, R. Bryer, and C. Farhat, "Miniaturized Autonomous Distributed Space Systems for Future Science and Exploration," *8th International Workshop of Spacecraft Formation Flying*, Delft University, 2015.

[2] D. C. Woffinden and D. K. Geller, "Observability Criteria for Angles-Only Navigation," *IEEE Transactions on Aerospace and Electronic Systems*, Vol. 45, No. 3, 2009, pp. 1194–1208.

[3] G. Gaias, S. D'Amico, and J.-S. Ardaens, "Angles-Only Navigation to a Noncooperative Satellite Using Relative Orbital Elements," *Journal of Guidance, Control, and Dynamics*, Vol. 37, No. 2, 2014, pp. 439–451, DOI: 10.2514/1.61494.

[4] D. C. Woffinden and D. K. Geller, "Optimal Orbital Rendezvous Maneuvering for Angles-Only Navigation," *Journal of Guidance, Control, and Dynamics*, Vol. 32, No. 4, 2009, pp. 1382–1387, DOI: 10.2514/1.45006.

[5] J. Sullivan, A. Koenig, and S. D'Amico, "Improved Maneuver-Free Approach to Angles-Only Navigation for Space Rendezvous," *26th AAS/AIAA Space Flight Mechanics Conference*, Napa, California, 2016.

[6] S. D'Amico, J.-S. Ardaens, G. Gaias, H. Benninghoff, B. Schlepp, and J. L. Jorgensen, "Noncooperative Rendezvous Using Angles-Only Optical Navigation: System Design and Flight Results," *Journal of Guidance, Control, and Dynamics*, Vol. 36, No. 6, 2013, pp. 1576–1595, DOI: 10.2514/1.59236.

[7] G. Gaias, J.-S. Ardaens, and S. D'Amico, "The Autonomous Vision Approach Navigation and Target Identification (AVANTI) Experiment: Objectives and Design," *9th International ESA Conference on Guidance, Navigation & Control Systems*, Porto, Portugal, 2014.

[8] S. D'Amico and O. Montenbruck, "Proximity Operations of Formation-Flying Spacecraft Using an Eccentricity/Inclination Vector Separation," *Journal of Guidance, Control, and Dynamics*, Vol. 29, No. 3, 2006, pp. 554–563, DOI: 10.2514/1.15114.

[9] D. Geller and T. A. Lovell, "Non-Iterative Approximate Solution to the Angles-Only Initial Relative Orbit Determination Problem in Spherical Coordinates," *AIAA/AAS Space Flight Mechanics Conference*, Napa, California, 2016.

[10] L. M. Hebert, "Angles-Only Initial Relative-Orbit Determination via Successive Maneuvers," Master's thesis, Auburn University, 2016.

[11] R. E. Kalman, "A New Approach to Linear Filtering and Prediction Problems," *Journal of Basic Engineering*, Vol. 82, No. 1, 1960, pp. 35–45.

[12] R. E. Kalman and R. S. Bucy, "New Results in Linear Filtering and Prediction Theory," *Journal of Basic Engineering*, Vol. 83, No. 1, 1961, pp. 95–108.

[13] R. E. Kalman, "New Methods in Wiener Filtering Theory," *Proceedings of the First Symposium on Engineering Applications of Random Function Theory and Probability*, 1963.

[14] R. S. Bucy, "Linear and Nonlinear Filtering," *Proceedings of IEEE*, Vol. 58, No. 6, 1970, pp. 854–864.

[15] S. J. Julier and J. K. Uhlmann, "New Extension of the Kalman Filter to Nonlinear Systems," *International Society for Optics and Photonics Conference*, 1997, pp. 182–193.

[16] J. Sullivan, S. Grimberg, and S. D'Amico, "A Comprehensive Survey and Assessment of Spacecraft Relative Motion Dynamics Models," *Journal of Guidance, Control, and Dynamics*, 2016. Accepted.

[17] A. Koenig, T. Guffanti, and S. D'Amico, "New State Transition Matrices for Relative Motion of Spacecraft Formations in Perturbed Orbits," *Journal of Guidance, Control, and Dynamics*. Accepted.

[18] S. Spiridonova, "Formation Dynamics in Geostationary Ring," *Celestial Mechanics and Dynamical Astronomy*, Vol. 125, No. 4, 2016, pp. 485–500, DOI: 10.1007/s10569-016-9693-0.

[19] T. Guffanti, S. D'Amico, and M. Lavagna, "Long-Term Analytical Propagation of Satellite Relative Motion in Perturbed Orbits," *Journal of Guidance, Control, and Dynamics*. Submitted.

[20] S. D'Amico, *Autonomous Formation Flying in Low Earth Orbit*. PhD thesis, Delft University, 2010.

[21] G. Gaias, J.-S. Ardaens, and O. Montenbruck, "Model of J_2 Perturbed Satellite Relative Motion with Time-Varying Differential Drag," *Celestial Mechanics and Dynamical Astronomy*, Vol. 123, No. 4, 2015, pp. 411–433, DOI: 10.1007/s10569-015-9643-2.

[22] J. Sullivan and S. D'Amico, "Nonlinear Kalman Filtering for Improved Angles-Only Navigation Using Relative Orbital Elements," *Journal of Guidance, Control and Dynamics*, 2017. Submitted.

[23] H. Schaub and J. L. Junkins, *Analytical Mechanics of Space Systems*. AIAA Education Series, 2003.

[24] D.-W. Gim and K. T. Alfriend, "State Transition Matrix of Relative Motion for the Perturbed Noncircular Reference Orbit," *Journal of Guidance, Control, and Dynamics*, Vol. 26, No. 6, 2003, pp. 956–971, DOI: 10.2514/2.6924.

[25] D.-W. Gim and K. T. Alfriend, "Satellite Relative Motion Using Differential Equinoctial Elements," *Celestial Mechanics and Dynamical Astronomy*, Vol. 92, No. 4, 2005, pp. 295–336, DOI: 10.1007/s10569-004-1799-0.

[26] D. Eddy, V. Giralo, and S. D'Amico, "Development and Verification of the Stanford GNSS Navigation Testbed for Spacecraft Formation-Flying," *9th International Workshop on Satellite Constellations and Formation Flight*, Boulder, Colorado, 2017.

[27] S. Palo, G. Stafford, and A. Hoskins, "An Agile Multi-Use Nano Star Camera for Constellation Applications," *27th Annual AIAA/USU Conference on Small Satellites*, Logan, Utah, 2013.

[28] M. Farahmand, A. Long, and R. Carpenter, "Magnetospheric Multiscale Mission Navigation Performance Using the Goddard Enhanced Onboard Navigation System," *Proceedings of the 25th International Symposium on Space Flight Dynamics*, 2015.

[29] R. Mehra, "Approaches to Adaptive Filtering," *1970 IEEE Symposium on Adaptive Processes (9th) Decision and Control*, No. 9, 1970, p. 141.

[30] R. Mehra, "On the Identification of Variances and Adaptive Kalman Filtering," *IEEE Transactions on automatic control*, Vol. 15, No. 2, 1970, pp. 175–184.

[31] K. Myers and B. Tapley, "Adaptive Sequential Estimation with Unknown Noise Statistics," *IEEE Transactions on Automatic Control*, Vol. 21, No. 4, 1976, pp. 520–523.

[32] P. S. Maybeck, R. L. Jensen, and D. A. Harnly, "An Adaptive Extended Kalman Filter for Target Image Tracking," *IEEE Transactions on Aerospace and Electronic Systems*, No. 2, 1981, pp. 173–180.

[33] R. Mehra, S. Seereeram, D. Bayard, and F. Hadaegh, "Adaptive Kalman Filtering, Failure Detection and Identification for Spacecraft Attitude Estimation," *Control Applications, 1995., Proceedings of the 4th IEEE Conference on*, IEEE, 1995, pp. 176–181.

[34] F. D. Busse, J. P. How, and J. Simpson, "Demonstration of Adaptive Extended Kalman Filter for Low-Earth-Orbit Formation Estimation Using CDGPS," *Journal Navigation*, Vol. 50, No. 2, 2003, pp. 79–93.

[35] N. J. Higham, "Computing a Nearest Symmetric Positive Semidefinite Matrix," *Linear algebra and its applications*, Vol. 103, 1988, pp. 103–118.